

Gravitational Lensing in Clusters of Galaxies

Makoto HATTORI,^{1,*} Jean-Paul KNEIB^{2,**} and Nobuyoshi MAKINO^{3,***}

¹ *Astronomical Institute, Tohoku University, Sendai 980-8578, Japan*

² *OMP, 14 Av. E. Belin, 31400 Toulouse, France*

³ *Oita National College of Technology, 1666 Maki, Oita 870-0152, Japan*

(Received March 12, 1999)

Gravitational lensing in clusters of galaxies is an efficient tool to probe the mass distribution of galaxies and clusters, high redshift objects thanks to the gravitational amplification, and the geometry of the universe. We review some important aspects of cluster lensing and related issues in *observational* cosmology.

§1. Introduction: Discovery of giant luminous arcs

More than a dozen years ago, the discovery of extremely elongated and luminous arc-like images in three distant rich clusters of galaxies A370, A2218 and CL2244-02 was reported by Lynds and Petrosian¹⁾ in the Bulletin of the American Astronomical Society. Independently, Soucail et al.²⁾ (see Fig. 1) discovered many arcs in the cluster A370 ($z = 0.37$). Soon after, Soucail et al.³⁾ measured a redshift of $z = 0.724$ for the giant arc in A370 — nearly twice the redshift of the lensing cluster — thus confirming the gravitational nature of the arc, as suggested by Paczyński.⁴⁾ Giant luminous arcs (GLA) are typically bluer, longer and generally brighter than (normal) cluster galaxies.

These discoveries have promoted gravitational lensing to the position of a major cosmological tool for the following purposes: i) study the cluster mass distribution; ii) probe high redshift galaxies using clusters as natural gravi-

Fig. 1. The discovery of the Giant Luminous Arc. An arc-like structure (A0) appeared on the CCD image of central part of cluster A370 at $z = 0.374$.²⁾ The image was taken during autumn, 1985, with a 320×512 pixels CCD using the Canada-France-Hawaii-Telescope (CFHT). The pixel size was ~ 0.8 arcsec. The strange blotch at position $\sim (-20, 30)$ is a CCD defect in the original CCD.

*) E-mail address: hattori@astr.tohoku.ac.jp

**) E-mail address: jean-paul.kneib@ast.obs-mip.fr

***) E-mail address: makino@astro.oita-ct.ac.jp

tational telescopes; iii) constrain the geometry of the universe, as parameterized by Ω_0 and Λ_0 , and especially the value of the cosmological constant; and iv) search for large-scale structures in the high redshift universe. This emerging new area seems to represent the realization of Zwicky’s^{5), 6)} dreams.

In this paper, we present the status of gravitational lensing studies of clusters of galaxies in regard to the above four topics — except the status of the weak lensing mass reconstruction, which is reviewed in another paper in this volume.⁷⁾

This review is organized as follows. Section 2 gives the fundamentals of gravitational lensing in order to understand how the cluster mass distribution can be constrained in the strong lensing regime. This description is restricted to key equations, since several very good reviews on lensing fundamentals have been published. The reader who is not familiar with the field of gravitational lensing can consult the reviews by Blandford and Kochanek,⁸⁾ Blandford and Narayan,⁹⁾ Schneider, Ehlers and Falco,¹⁰⁾ Fort and Mellier,¹¹⁾ Wu¹²⁾ and Narayan and Bertelmann¹³⁾ and Mellier.¹⁴⁾ Section 3 presents an overview of the modelling of the mass distribution in clusters in the strong lensing regime, with a comparison between the lensing and X-ray mass estimates. Indeed, a discrepancy of a factor of 2–3 is generally observed between strong lensing and de-projection of the X-ray emission of the intra-cluster medium (henceforth ICM). Proposed solutions to this problem are summarized. Section 4 discusses the “dark” lens problem in connection to the search for very high redshift clusters. Section 5 presents recent applications of the use of clusters of galaxies as natural gravitational telescopes to study the nature of high redshift galaxies. Section 6 summarizes the studies connecting the statistics of lensed galaxies in clusters, nicknamed “arc statistics”. Arc statistics are sensitive to: i) the cosmological world models (and particularly to Ω_0 and Λ_0); ii) the average cluster mass distribution/profile; and iii) the nature and evolution of high redshift galaxies. Clearly, arc statistics depend on a large number of parameters. We therefore attempt here to clarify its possible application in order to sharpen focus of considerations on its future use. Section 7 summarizes the proposed ideas to constrain the geometry of the universe by using the lensing effect due to clusters of galaxies. In each section, we attempt to explain how the new generation of telescopes and instruments (SUBARU, VLT, Gemini, Astro-E, AXAF, XMM, NGST, LSA/MMA, LMSA ...) may enrich the cluster-lensing subject.

This review focuses on various aspects (particularly those we have been deeply involved with) and should not be considered exhaustive. However, we believe that this focus makes this review unique from others and that it will help readers to catch up quickly with the current frontier of this subject.

§2. Fundamentals of cluster lensing

Gravitational lensing theory is based on the limit of a weak stationary gravitational field. Furthermore, in the case of cluster lensing, the size of the deflector is much smaller than the light propagation distance. Therefore, the lens can be safely approximated by a single plane of matter with a projected surface mass density $\Sigma(\vec{\theta})$ — usually referred as the *thin lens approximation*. All our discussion is based on

these assumptions.

2.1. Definition of an arc

General relativity states that the presence of massive object distorts space-time. Thus propagating light beams coming from distant sources will be sensible to any mass inhomogeneities ‘en route’. The light coming from any extended sources and passing through a massive cluster of galaxies will therefore suffer major distortions and amplifications due to the gravitational lensing effect. In some extreme cases, the distortions are non-linear (on the scale of the image), and the image is strongly curved, having no doubt as to the gravitational nature of the image. Such lensed images are usually called “arc”, yet it is clearly a subjective definition. In this paper, to quantify the definition of a lensed image, we use the term *arc* for images with an axis ratio (length-to-width) larger than 10, and *arclet* for images with length-to-width ratios between 2 and 10. Furthermore, giant arcs brighter than $V = 22.5$ are defined as *giant luminous arc* (GLA), following the definition of Le Fèvre et al.¹⁵⁾

2.2. Lensing equation: Mapping and deformation

The lensing equation can simply be expressed as a mapping from the image plane to the source plane. For an angular position of the image $\vec{\theta}$, the angular position of the source $\vec{\beta}$ is given by the lensing equation

$$\vec{\beta} = \vec{\theta} - \vec{\nabla}_{\theta}\psi(\theta), \quad (2.1)$$

where $\psi(\theta)$ is the effective lensing potential and $\vec{\nabla}_{\theta}$ is the 2D gradient by $\vec{\theta}$. It is important to realize that this equation may admit multiple solutions in $\vec{\theta}$ for a fixed $\vec{\beta}$, depending on the values of the potential ψ . If multiple solution exists, we will say that the lens produces multiple images of a source at position $\vec{\beta}$; this domain defines the strong lensing regime (see below).

The effective lensing potential ψ is defined by the Poisson equation,

$$\vec{\nabla}_{\theta}^2 \psi = 2 \frac{\Sigma(\vec{\theta})}{\Sigma_{\text{cr}}} \equiv 2\kappa(\vec{\theta}), \quad (2.2)$$

where Σ_{cr} is the critical surface mass density defined by

$$\Sigma_{\text{cr}} = \frac{c^2}{4\pi G} \frac{D_s}{D_d D_{\text{ds}}}. \quad (2.3)$$

The surface mass density normalized by the critical surface mass density is called the ‘convergence’ $\kappa(\vec{\theta})$. The effective lensing potential can be obtained by solving the Poisson equation (2.2):

$$\psi(\vec{\theta}) = \frac{1}{\pi} \int \kappa(\vec{\theta}') \ln|\vec{\theta} - \vec{\theta}'| d^2\theta'. \quad (2.4)$$

A surface element of the image plane $\delta\vec{\theta}$ is related to a surface element of the source plane $\delta\vec{\beta}$ via the inverse of the magnification matrix A , defined by

$$\delta\vec{\beta} = \frac{\partial\vec{\beta}}{\partial\vec{\theta}}\delta\vec{\theta} = \left(I - \vec{\nabla}_{\theta}\vec{\nabla}_{\theta}\psi\right)\delta\vec{\theta} = A^{-1}\delta\vec{\theta}, \quad (2.5)$$

where $\vec{\nabla}_\theta \vec{\nabla}_\theta$ is 2×2 diadictensor and I is 2×2 unit matrix. The magnification matrix can be written as a function of the second derivatives of the potential. In Cartesian coordinates, it reads

$$A^{-1} = \begin{pmatrix} 1 - \frac{\partial^2 \psi}{\partial \theta_x^2} & -\frac{\partial^2 \psi}{\partial \theta_x \partial \theta_y} \\ \frac{\partial^2 \psi}{\partial \theta_x \partial \theta_y} & 1 - \frac{\partial^2 \psi}{\partial \theta_y^2} \end{pmatrix}, \quad (2.6)$$

and in polar coordinates,

$$A^{-1} = \begin{pmatrix} 1 - \frac{\partial^2 \psi}{\partial \theta^2} & -\frac{\partial}{\partial \theta} \left(\frac{1}{\theta} \frac{\partial \psi}{\partial \varphi} \right) \\ -\frac{\partial}{\partial \theta} \left(\frac{1}{\theta} \frac{\partial \psi}{\partial \varphi} \right) & 1 - \frac{1}{\theta} \frac{\partial \psi}{\partial \theta} - \frac{1}{\theta^2} \frac{\partial^2 \psi}{\partial \varphi^2} \end{pmatrix}, \quad (2.7)$$

where $\theta = |\vec{\theta}|$, and φ is the azimuthal angle of the image position. Note surface elements of image and source planes should be taken as $\delta \vec{\theta} = (\delta \theta, \theta \delta \varphi)$ and $\delta \vec{\beta} = (\delta \beta, \beta \delta \varphi')$ in the polar coordinates, where $\beta = |\vec{\beta}|$ and φ' is the azimuthal angle of the source position.

In the limit of a single lens plane, the magnification matrix is real and symmetric. Thus in this limit it is diagonalizable. The transformation of a surface element is non-linear and can be expressed by two effects, an isotropic magnification expressed by the convergence κ and a deformation expressed by the complex shear $\bar{\gamma}$:

$$A^{-1} = \begin{pmatrix} 1 - \kappa - \gamma_1 & \gamma_2 \\ \gamma_2 & 1 - \kappa + \gamma_1 \end{pmatrix}, \quad (2.8)$$

where $\bar{\gamma} = \gamma_1 + i\gamma_2 = \gamma(\cos(2\theta_A) + i\sin(2\theta_A))$ with θ_A giving the shear direction.

In the shear coordinates, the magnification matrix is diagonal with proper values $1 - \kappa - \gamma$ and $1 - \kappa + \gamma$. The total magnification μ is defined by the determinant of the magnification matrix (when it is defined): $\mu = \det A = 1/((1 - \kappa)^2 - \gamma^2) \equiv H(\vec{\theta})^{-1}$, where $H(\vec{\theta})$ is the Hessian of the lens mapping. Depending on the sign of the total magnification μ , the parity of the image will change. For $\mu > 0$, the image has the same parity as the original source, even, while for $\mu < 0$, the image has mirror-symmetry compared to the original source, and the image parity is *odd*. The family of points for which the inverse of the magnification matrix is singular (infinite magnification: $\mu^{-1} = 0$) are called *critical lines*. They correspond to $\kappa + \gamma = 1$ (external) or $\kappa - \gamma = 1$ (internal). The corresponding curves in the source plane are called *caustic lines*.

For a non-uniform mass distribution, if $\Sigma(\theta)$ exceeds Σ_{cr} in a region of the image plane, it ensures that the equation $\mu^{-1} = 0$ admits a solution. Thus critical lines exist. Clusters with a surface mass density higher than the critical surface mass density are called *critical lenses*, and such a surface mass density is said to be *super critical*.

Arcs occur close to and across critical lines (as the merging of two or more “multiple images”). They are strongly deformed and highly magnified. The region in which arcs can be found is referred to as the *strong lensing* regime.

2.2.1. Case of a circular symmetric lens

Although the circular symmetric case is an unrealistic description of a cluster mass distribution, it is helpful to understand the gravitational lensing. We shall discuss it in more detail here.

Indeed, in the case of a circular symmetric lens, the lens equation reads

$$\beta(\theta) = \theta - \frac{M(\theta)}{\pi D_d^2 \theta \Sigma_{\text{cr}}}, \quad (2.9)$$

and the inverse of the magnification matrix is (in polar coordinates)

$$A^{-1} = \begin{pmatrix} \frac{d\beta}{d\theta} & 0 \\ 0 & \frac{\beta}{\theta} \end{pmatrix} = \begin{pmatrix} 1 - \frac{1}{\pi D_d^2 \Sigma_{\text{cr}}} \frac{\partial}{\partial \theta} \left(\frac{M(\theta)}{\theta} \right) & 0 \\ 0 & 1 - \frac{1}{\pi D_d^2 \Sigma_{\text{cr}}} \left(\frac{M(\theta)}{\theta^2} \right) \end{pmatrix}, \quad (2.10)$$

where $M(\theta)$ is the lens mass enclosed within a radius $D_d \theta$,

$$M(\theta) = 2\pi D_d^2 \int_0^\theta \Sigma(\theta') \theta' d\theta'. \quad (2.11)$$

The factor $\frac{\theta}{\beta}$ in (2.10) is the tangential deformation factor of the image. This can easily be understood by geometrical considerations. In the case of a circular symmetric lens, a light ray can only be radially displaced. Now, consider a (small) source at position β from the centre of the mass distribution with a length l in the tangential direction. Its image is located at position θ with a tangential length $l' = l \times (\frac{\theta}{\beta})$, as only radial displacements are allowed. Similarly, $(\frac{d\beta}{d\theta})^{-1}$ is the deformation factor of the image in the radial direction, because this is the ratio of the unlensed source width, $\delta\beta$, to the lensed image width, $\delta\theta$.

When the surface mass density follows a power law of the form $\Sigma(\theta) = C_0 \theta^{-\delta}$ with $\delta < 2$, the magnification matrix can be written as

$$A^{-1} = \begin{pmatrix} 1 - \frac{2C_0}{\Sigma_{\text{cr}}} \left(\frac{1-\delta}{2-\delta} \right) \frac{1}{\theta^\delta} & 0 \\ 0 & 1 - \frac{2C_0}{\Sigma_{\text{cr}}} \frac{1}{2-\delta} \frac{1}{\theta^\delta} \end{pmatrix}. \quad (2.12)$$

In the circular case, critical lines are easily defined, by symmetry considerations; they are circles. The tangential (external) critical curve given by $\beta/\theta = 0$ is a circle, called an ‘Einstein ring’. The Einstein radius is defined by

$$\theta_E = \frac{1}{D_d} \left(\frac{M(\theta_E)}{\pi \Sigma_{\text{cr}}} \right)^{1/2}. \quad (2.13)$$

The radial deformation factor at the Einstein radius is

$$\left(\frac{d\beta}{d\theta} \right)^{-1} = \left[2 \left(1 - \frac{\Sigma(\theta_E)}{\Sigma_{\text{cr}}} \right) \right]^{-1}. \quad (2.14)$$

When the surface mass density follows a power law of the form $\Sigma(\theta) \propto \theta^{-\delta}$, the radial deformation factor can be written as

$$\left(\frac{d\beta}{d\theta} \right)^{-1} = \frac{1}{\delta}. \quad (2.15)$$

Therefore, for a lens with $\delta = 1$, which corresponds to the SIS model, the radial deformation factor is unity, while a more compact mass distribution ($\delta > 1$) forms narrower arcs (the radial stretching rate is less than 1), and a shallower mass distribution ($\delta < 1$) produces thicker arcs (the radial stretching rate is larger than 1).

The radial (internal) critical curve given by $d\beta/d\theta = 0$ is either a point (if the mass distribution is singular) or a circle of radius

$$\theta_{\text{R}} = \frac{1}{D_{\text{d}}} \left(\frac{M(\theta_{\text{R}})}{\pi \Sigma_{\text{cr}}} \right)^{\frac{1}{2}} \left(\frac{1}{\frac{2\Sigma(\theta_{\text{R}})}{\Sigma_{\text{cr}}} - 1} \right)^{\frac{1}{2}}. \quad (2.16)$$

When $\Sigma(\theta) \propto \theta^{-\delta}$, the convergence and the tangential deformation factor at the radial critical radius are given by

$$\kappa(\theta_{\text{R}}) = \frac{1}{2} \left(\frac{2 - \delta}{1 - \delta} \right), \quad (2.17)$$

$$\left| \frac{\theta}{\beta} \right| = \left| 1 - \frac{1}{\delta} \right|. \quad (2.18)$$

Equation (2.17) shows that $\delta < 1$ is required for a lens to have a radial critical line, since the convergence must be positive. Equation (2.18) shows that for a lens with $\delta = 0.5$, the tangential deformation factor is unity, while a more compact mass distribution ($1 > \delta > 0.5$) forms thinner arcs and a shallower mass distribution. The case $\delta < 0.5$ produces thicker arcs.

If the source position is slightly off of centre, the ring is split into two tangential highly stretched arc lying close to the Einstein ring. The typical angular separation of images is of order $2\theta_{\text{E}}$. Therefore, if a pair of arcs or multiply imaged arcs are found in the cluster core, the Einstein radius can be estimated from the distance between the arc and cluster centre, and a very crude estimation of the mass of the cluster within the Einstein radius can be estimated by

$$M(\theta_{\text{E}}) = \pi \theta_{\text{E}}^2 \Sigma_{\text{cr}}. \quad (2.19)$$

The critical surface density Σ_{cr} is obtained by measuring the redshifts of the lens cluster, z_{d} , and source, z_{s} , by fixing the values of Ω_0 , A_0 and H_0 . For example, for $z_{\text{s}} = 1$ and $z_{\text{d}} = 0.3$ with $(\Omega_0, A_0, H_0) = (1.0, 0.0, 100 \text{ km/sec/Mpc})$, we have

$$\Sigma_{\text{cr}} = 1.09 h^{-1} \text{ g/cm}^2, \quad (2.20)$$

which is of the order of the weight of a sheet of paper.

Before the discovery of giant arcs, the Coma cluster was the archetype of a rich cluster of galaxies. The central surface mass density of the Coma estimated from its X-ray emission, assuming spherical symmetry and isothermal hydrostatic equilibrium, is given by

$$\Sigma_{\text{Coma}}(0) = \frac{3}{2G} \beta \frac{k_{\text{B}} T}{\mu m_{\text{H}}} = 0.37 \left(\frac{kT}{8.3 \text{ keV}} \right) \left(\frac{\beta}{0.75} \right) \left(\frac{r_c}{200 h^{-1} \text{ kpc}} \right)^{-1} \text{ g cm}^{-2}, \quad (2.21)$$

where the electron density is assumed to be described by $n_e(r) = n_e(0)(1 + (\frac{r}{r_c})^2)^{-\frac{3}{2}\beta}$. Since this value is smaller than the critical surface mass density, it was believed that clusters of galaxies could not produce strong lensing events. Clearly, the discovery of giant arcs has revolutionized the view we had of the mass distribution of cluster cores.

2.2.2. Spherical lens models

The analytical formulae of frequently used spherically symmetric mass distribution models are summarized in this subsection.

• *Singular isothermal sphere (SIS) model*

A singular isothermal sphere (SIS) is a solution of the collisionless Boltzmann equation. The word “isothermal” means here that the velocity dispersion of the system is isotropic and uniform. SIS is frequently used in lensing analysis, since the density profile of SIS is very simple, and most quantities related to gravitational lensing are described in simple analytic forms. It is instructive to examine lensing properties using SIS (see, for example, Turner, Ostriker and Gott III¹⁶).

The mass density of SIS is described by

$$\begin{aligned}\rho(r) &= \rho_0 \left(\frac{r_0}{r}\right)^2 \\ &= \frac{\sigma^2}{2\pi G r^2},\end{aligned}\tag{2.22}$$

where r_0 is the scaling parameter, ρ_0 is the mass density at r_0 , and σ^2 is the line of sight velocity dispersion.

Integrating the above equation along the line of sight, one obtains the surface density of the singular isothermal sphere at an angle θ ,

$$\Sigma(\theta) = \frac{\sigma^2}{2GD_d\theta}.\tag{2.23}$$

The lens mass enclosed within a radius $D_d\theta$, is found to be

$$M(\theta) = \frac{\pi\sigma^2 D_d\theta}{G}.\tag{2.24}$$

Although the mass within a finite radius does not diverge, the central density and the total mass diverge. Therefore this model is not a physical representative of a realistic mass distribution and should only be considered as a simple model to quickly estimate physical parameters.

• *Isothermal sphere with a finite core radius*

To avoid the divergence found in SIS, a finite core can be added. The density profile of an isothermal sphere with a finite core radius is therefore defined by

$$\rho(r) = \rho_0 \left(1 + \frac{r^2}{r_c^2}\right)^{-1},\tag{2.25}$$

where ρ_0 is the density at the centre, and r_c is the core radius.

The surface density of an isothermal sphere with a finite core radius is

$$\Sigma(\theta) = \frac{\pi\rho_0 D_d \theta_c^2}{\sqrt{\theta^2 + \theta_c^2}}, \quad (2.26)$$

where $\theta_c = r_c/D_d$. The mass enclosed within the radius θ is

$$M(\theta) = 2\pi^2 D_d^3 \rho_0 \theta_c^2 \left(\sqrt{\theta^2 + \theta_c^2} - \theta_c \right). \quad (2.27)$$

Similarly as the SIS, lensing quantities of an isothermal sphere with a finite core radius are also described by simple analytic functions. However, the total mass of this model is still infinite.

• *Modified Hubble law*

The modified Hubble law is used as an analytical approximation of the King model, which is one of the solutions of the collisionless Boltzmann equation. The King model can be approximated at small radius by the modified Hubble law.

The mass density profile of the modified Hubble law is given by

$$\rho(r) = \rho_0 \left(1 + \frac{r^2}{r_c^2} \right)^{-3/2}, \quad (2.28)$$

where ρ_0 is the density at the centre, and r_c is the core radius. Integrating the density distribution along the line of sight, one can obtain the surface density

$$\Sigma(\theta) = \frac{2\rho_0 D_d \theta_c^3}{\theta^2 + \theta_c^2}. \quad (2.29)$$

The projected mass of the modified Hubble law is

$$M(\theta) = 2\pi D_d^3 \theta_c^3 \rho_0 \log \left(\frac{\theta^2 + \theta_c^2}{\theta_c^2} \right). \quad (2.30)$$

Since the mass density vanishes in the limit $r \rightarrow \infty$ faster than SIS, it is difficult to produce strong lensing events for a finite mass unless it is extremely compact and massive. The modified Hubble model was conventionally used in describing a galaxy distribution in a cluster.

• *Isothermal β -model*

It is empirically known that (generally) the radial profile of the X-ray surface brightness can be described well by the so-called β -model among X-ray astronomers, that is,

$$S_x(r) = S_0 \left[1 + \frac{r^2}{r_c^2} \right]^{-3\beta+1/2}. \quad (2.31)$$

If the intra-cluster gas is isothermal (the gas temperature is constant throughout the cluster), and in hydrostatic equilibrium, the electron density profile is obtained from

this formula as $n_e(r) = n_e(0)(1 + (r/r_c)^2)^{-3\beta/2}$. Then we can solve the hydrostatic equation to obtain the cluster mass distribution. The mass density distribution of the isothermal β -model is given by

$$\rho(r) = \rho_0 \frac{3 + (r/r_c)^2}{[1 + (r/r_c)^2]^2}, \quad (2.32)$$

where r_c is the core radius. The parameter ρ_0 is determined from X-ray observations by fitting the β -model to the X-ray surface brightness. It is given by

$$\rho_0 = \frac{3\beta k_B T}{4\pi G \mu m_H r_c^2}, \quad (2.33)$$

where β is the slope parameter in the β -model, k_B is the Boltzmann constant, T is the temperature of the X-ray emitting gas, μ is the mean molecular weight, and m_H is the Hydrogen mass. The surface density is

$$\Sigma(\theta) = \pi \rho_0 D_d \frac{\theta_c^2 (2\theta_c^2 + \theta^2)}{(\theta_c^2 + \theta^2)^{3/2}}. \quad (2.34)$$

The projected mass of the isothermal β -model is

$$M(\theta) = 2\pi^2 D_d^3 \rho_0 \theta_c^2 \frac{\theta^2}{\sqrt{\theta_c^2 + \theta^2}}. \quad (2.35)$$

The temperature required to have an Einstein ring radius of θ_E is written as

$$k_B T = \frac{1}{6\pi\beta} \mu m_H c^2 \frac{D_s}{D_{ds}} \sqrt{\theta_E^2 + \theta_c^2}. \quad (2.36)$$

This formula is useful to check whether X-ray results are consistent with strong lensing mass estimates, assuming that the mass distribution is spherical.

- *NFW profile*

The NFW universal density profile is a fit of a *relaxed system* simulated by N -body simulations with a high resolution.¹⁷⁾ According to Navarro, Frenk and White,¹⁷⁾ all profiles found in the simulations have the same shape, independent of the halo mass, initial density fluctuation spectrum, and values of the cosmological parameters. (For these reasons it was called ‘universal’.)

The NFW density profile is given by

$$\rho(r) = \frac{\rho_{cr} \delta_c}{\frac{r}{r_s} \left(1 + \frac{r}{r_s}\right)^2}, \quad (2.37)$$

where ρ_{cr} is the critical density, δ_c is the density parameter, and r_s is the scaling parameter.

One obtains the surface density by integrating the mass density along the line of sight. The surface mass density is, for $\theta < \theta_s (= r_s/D_d)$,

$$\Sigma(\theta) = 2\rho_0 D_d \theta_s \left[\frac{2\theta_s^3}{(\theta_s^2 - \theta^2)^{3/2}} \operatorname{arctanh} \sqrt{\frac{\theta_s - \theta}{\theta_s + \theta}} - \frac{\theta_s^2}{\theta_s^2 - \theta^2} \right], \quad (2.38)$$

for $\theta = \theta_s$,

$$\Sigma(\theta) = \frac{2}{3}\rho_0\theta D_d, \quad (2.39)$$

and for $\theta > \theta_s$,

$$\Sigma(\theta) = 2\rho_0 D_d \theta_s \left[-\frac{2\theta_s^3}{(\theta^2 - \theta_s^2)^{3/2}} \arctan \sqrt{\frac{\theta - \theta_s}{\theta + \theta_s}} + \frac{\theta_s^2}{\theta^2 - \theta_s^2} \right], \quad (2.40)$$

where $\rho_0 = \delta_c \rho_{\text{cr}}$. For $\theta/\theta_s < 10^{-3}$, $\Sigma \propto \theta^{-0.1}$. For $10^{-3} < \theta/\theta_s < 10^{-1}$, $\Sigma \propto \theta^{-0.4}$. For $10^{-1} < \theta/\theta_s < 0.3$, $\Sigma \propto \theta^{-0.6}$. For $0.3 < \theta/\theta_s < 1$, $\Sigma \propto \theta^{-0.95}$. For $1 < \theta/\theta_s < 10$, $\Sigma \propto \theta^{-1.5}$. For $10 < \theta/\theta_s$, $\Sigma \propto \theta^{-2}$.

The projected mass for $\theta < \theta_s$ is

$$M(\theta) = 4\pi\rho_0 D_d^3 \theta_s^3 \left[\log \frac{\theta}{2\theta_s} + \frac{2\theta_s}{\sqrt{\theta_s^2 - \theta^2}} \operatorname{arctanh} \sqrt{\frac{\theta_s - \theta}{\theta_s + \theta}} \right], \quad (2.41)$$

for $\theta = \theta_s$,

$$M(\theta) = 4\pi\rho_0 D_d^3 \theta_s^3 \left(\log \frac{\theta}{2\theta_s} + 1 \right), \quad (2.42)$$

and for $\theta > \theta_s$,

$$M(\theta) = 4\pi\rho D_d^3 \theta_s^3 \left[\log \frac{\theta}{2\theta_s} + \frac{2\theta_s}{\sqrt{\theta^2 - \theta_s^2}} \arctan \sqrt{\frac{\theta - \theta_s}{\theta + \theta_s}} \right]. \quad (2.43)$$

The formulae for the NFW density profile are found in Bartelmann¹⁸⁾ and Maoz et al.¹⁹⁾

2.2.3. Pseudo-elliptical lensing potential

If one would like to construct a physically motivated cluster mass model, one should start from the 3D mass distribution. However, as long as the mass distribution of the lens is thin enough to be described sufficiently well by the *thin lens approximation*, only the surface mass density affects the lensing phenomena. Furthermore, it is usually complicated to construct the projected mass distribution and its lensing properties' model based on a realistic 3D mass distribution even for an ellipsoidal mass distribution (see the next subsection). Therefore, the elliptical surface mass density distribution and the elliptical lensing potential have been widely used in lens modelling because they provide simple analytic descriptions of physically motivated mass models. In this subsection, the nature of the non-singular pseudo-elliptical lensing potential Eq. (2.44) is summarized, since it has been widely used for lens modelling, and the behavior of the arcs produced by the pseudo-elliptical lensing potential illustrates typical elliptical lensing configurations.

The non-singular pseudo-elliptical lensing potential is defined by

$$\psi(\vec{\theta}) = \frac{D_{\text{ds}}}{D_s} 4\pi \frac{\sigma_v^2}{c^2} [\theta_0^2 + (1 - \epsilon)\theta_1^2 + (1 + \epsilon)\theta_2^2]^{1/2}, \quad (2.44)$$

where $\epsilon = (a^2 - b^2)/(a^2 + b^2)$ is the ellipticity of the potential. The ellipticity of the projected mass density is $\sim 3\epsilon$ for small ϵ .²⁰⁾ When $\epsilon = 0$ and $\theta_0 = 0$, σ_v is exactly

the line-of-sight velocity dispersion (1D velocity dispersion) of a singular isothermal sphere, and it is a constant throughout the cluster.

However, in the case of a finite core radius, interpretation of σ_v requires caution. In the circular potential limit ($\epsilon = 0$), σ_v can be related to the 1D central velocity dispersion of the original 3D mass distribution,²⁰⁾ σ_0 , by assuming an isotropic velocity distribution, self-gravitating spherical equilibrium system such as

$$\sigma_0^2 = \frac{2}{3}\sigma_v^2. \quad (2.45)$$

These are related to the central line-of-sight velocity dispersion,²⁰⁾ σ_{los} :

$$\sigma_{\text{los}}^2(0) = \frac{9}{8}\sigma_0^2 = \frac{3}{4}\sigma_v^2. \quad (2.46)$$

They are also related to X-ray observables⁶⁴⁾ by

$$\sigma_0^2 = \frac{2}{3}\sigma_v^2 = \beta \frac{k_{\text{B}}T}{\mu m_{\text{H}}}, \quad (2.47)$$

where the isothermal β model is used for modelling the cluster mass distribution.

The non-singular pseudo-elliptical lensing potential should be used with caution, because for $|\theta_2| \gg |\theta_1| \gg \theta_0$ the mass-isodensity contours are convex only if $|\epsilon| < 1/5$. For $\epsilon > 1/5$, the mass-isodensity has a complex shape, something like a dumbbell.²¹⁾

The ellipticity of the mass distribution of a self-gravitating non-rotating collisionless system (which is likely to be the case for cluster of galaxies) is limited by the dynamical instability,²²⁾ and the axis ratio must be smaller than $a/b \sim 2.5$. Thus we expect that in many cases the elliptical potential cannot be a good representation of a physically motivated mass distribution.

2.2.4. Elliptical mass distribution

In this subsection, we first consider the lensing due to an oblate spheroidal as an example of a 3D ellipsoidal mass distribution of the lens.²³⁾ The density distribution of the oblate spheroidal is described by $\rho(a)$, where a is defined by

$$a^2 \equiv x'^2 + y'^2 + \frac{z'^2}{1-e^2} \quad \text{for } 1 > e \geq 0. \quad (2.48)$$

When the symmetry axis z' is tilted relative to the line of sight by an angle γ , the 2D surface mass density is described by

$$\Sigma(x_i, y_i) = \sqrt{\frac{1-e^2}{1-e^2\sin^2\gamma}} \int_{b^2}^{r_{\text{cut}}^2} da^2 \frac{\rho(a)}{\sqrt{a^2-b^2}}, \quad (2.49)$$

where r_{cut} is the cut off radius of the cluster mass distribution in the direction of the major axis of the oblate spheroid, x_i and y_i are coordinates in the lens plane, which is perpendicular to the line of sight, and b is defined by

$$b^2 \equiv x_i^2 + \frac{y_i^2}{1-e^2\sin^2\gamma}. \quad (2.50)$$

The complex formulation of the lensing equation is convenient in this case, and the lensing equation is written as

$$Z_s = Z - \frac{1}{\pi} I^*(Z), \quad (2.51)$$

where $Z_s \equiv x_s + iy_s$ is the source position, $Z \equiv x_i + iy_i$ is the image position in complex form, and I^* is the complex conjugate of the scattering function, $I(Z)$, which is defined by

$$I \equiv \int dx'_i dy'_i \kappa(b') \frac{1}{Z - Z'} = 2\pi \frac{\sqrt{Z^2}}{Z} \sqrt{1 - e^2 \sin^2 \gamma} \int_0^{\min(r_{\text{cut}}, b)} db' \frac{b' \kappa(b')}{\sqrt{Z^2 - b'^2 e^2 \sin^2 \gamma}}. \quad (2.52)$$

A more detailed derivation of this equation is given by Asano and Fukuyama.²⁴⁾ This result shows that only the mass within the isodensity contour at the position of the image, b , contributes on the lensing equation.²⁴⁾

For example, an image positioned on the minor axis will be sensitive to the mass within an ellipse and thus with a larger area compared to the circular symmetric case. Therefore, an elliptical lens need not be super critical to have multiple images (see the next section).

We now discuss the properties of the pseudo-isothermal elliptical mass distribution, since it is one of the most useful elliptical surface density profiles, and has been extensively applied to the simple mass estimate of lens cluster.²⁵⁾ The convergence of the pseudo-isothermal elliptical mass profile is given by

$$\kappa(b) = \frac{\kappa_0 b_0}{\sqrt{b_0^2 + b^2}}, \quad (2.53)$$

where κ_0 is the convergence at the centre, and b_0 is the core radius. One obtains the scattering function I from Eq. (2.52) for Eq. (2.53) with $r_{\text{cut}} \rightarrow \infty$:

$$I(Z) = 2\pi \kappa_0 \theta_c \frac{\sqrt{Z^2}}{iZ} \sqrt{\frac{1 - e^2 \sin^2 \gamma}{e^2 \sin^2 \gamma}} \ln \left[\frac{i \sqrt{(b_0^2 + \theta_c^2) e^2 \sin^2 \gamma} + \sqrt{Z^2 - b_0^2 e^2 \sin^2 \gamma}}{i \theta_c \sqrt{e^2 \sin^2 \gamma - \sqrt{Z^2}}} \right]. \quad (2.54)$$

From the scattering function we can then easily compute the lensing properties of this mass distribution. Although this mass distribution does not have a finite total mass, a truncated version of that model can be constructed (see Kneib et al.³²⁾). The lens properties of the pseudo-isothermal elliptical mass profile are similar to those of the pseudo-elliptical lensing potential, in particular the behavior of image configurations.²⁵⁾ However, there are several qualitative differences between these two. A pseudo-isothermal elliptical mass distribution can have naked cusps for any value of the central convergence or the core radius, whereas a physically meaningful pseudo elliptical lens potential can only have naked cusps when $\kappa_0 < 5$. Since the convergence is given in the pseudo-isothermal elliptical mass profile, the contour of the isodensity is convex for all values of the ellipticity, and the surface density is always positive (which is not always the case for an elliptical potential).

2.3. Multiple images and time delay: Folds, cusps, lips and beak-to-beak caustics

When a light ray propagates through a deep gravitational field, the arrival time of the light to an observer is delayed by two effects: i) a geometrical effect and ii) a gravitational effect. The geometrical delay is explained by the deflection of the light by the gravitational field. The gravitational delay is due to the fact that a deep gravitational potential is equivalent to a medium with a refractive index $(1 + 2\phi/c^2)^{-1}$, which is larger than 1 (ϕ is the 3D gravitational potential defined so that at infinity $\phi=0$). Hence, the effective speed of light propagating through a deep gravitational potential is “slower” and results in a delay of the arrival time.

For a source at position $\vec{\beta}$ in the source plane, the time delay at position $\vec{\theta}$ in the image plane is given by²⁶⁾

$$t(\vec{\theta}) = \frac{(1 + z_d)}{c} \frac{D_d D_s}{D_{ds}} \left[\frac{1}{2} (\vec{\theta} - \vec{\beta})^2 - \psi(\vec{\theta}) \right], \quad (2.55)$$

where z_d is the redshift of the lens, D_s , D_d and D_{ds} are angular diameter distances of the observer to the source, the observer to the lens, and the lens to the source, respectively, and $\psi(\vec{\theta})$ is the effective gravitational lensing potential, which corresponds to the gravitational time delay. The effective gravitational lensing potential is defined by Eq. (2.4), and its amplitude depends both on the mass distribution of the lensing object and the distance to the source. The term $\frac{1}{2}(\vec{\theta} - \vec{\beta})^2$ corresponds to the geometrical effect. Fermat’s Principle states that a light ray follows a trajectory such that the light-travel time is stationary relative to neighboring trajectories. In other words, the images are located at those points where the time-delay surface $t(\vec{\theta})$ is stationary: $\vec{\nabla}_\theta t(\vec{\theta}) = 0$. This defines the lensing equation (2.1), where $\vec{\nabla}_\theta$ is the 2D gradient by $\vec{\theta}$.

The number of stationary points in the time-delay surface corresponds to the number of expected images. This number depends on the source position in the sky, the lensing parameter, which depends on the redshift of the lens and the source and depth and shape of the lens potential, and (Ω_0, A_0) through angular diameter distances. The behavior of the time-delay surface is described well by the catastrophe theory.²⁷⁾ In the case of lensing theory, the number of independent control parameters is three, e.g., two parameters for specifying the source position in the sky and one lensing parameter. Therefore, elementary catastrophes that play a role in lensing are folds, cusps, swallow tails, hyperbolic umbilics and elliptic umbilics.

For a circular symmetric lens, the nature of the time-delay potential depends only on the radial distance of the source position from the lens centre. In other words, the number of the control parameters is one. Therefore, Tom’s catastrophe theorem implies that only the fold catastrophe appears in a circular symmetric lens (Fig. 2). For an elliptical lens, the time-delay potential depends on the two-dimensional positions of the source, and hence the number of control parameters is two. Therefore, the cusp and fold catastrophe can appear in this case (Fig. 3). When a source crosses a fold caustic from inside to the outside, two images with opposite parity will become closer, then merges at the location of the critical line and finally disappear, when the source moves outside of the caustics. When a source crosses a cusp caustic

Fig. 2. The caustics and critical lines of a circular lens with a finite core. Left and right panels describe the caustics in the source plane and the critical lines in the image plane, respectively. A tangential (radial) caustic is a central point in the source plane, and the corresponding critical line is a outer circle in the image plane. The appearance of the images corresponding to each source position are also shown.

from the inside to the outside, three images with opposite parity will become closer, and then merge at the location of the critical line, and only one image with the same parity as the original source parity remains when the source moves outside of the caustics. If a cusp caustic lies outside the radial caustic as described in Fig. 3, such a cusp is termed “naked cusp.” If a source lies close to a naked cusp, one or three highly magnified images appear without any additional images. The first discovered giant arc in A370 is likely to be a highly magnified image due to a naked cusp (Fig. 9).

For simple gravitational lenses (with one main clump) we can distinguish between two types of caustics. Tangential caustics occur when the deformation of the merging images is tangential (nearly parallel to the critical line). Radial caustics occur when the deformation of the merging images is radial (nearly perpendicular to the critical line).

Detection of a radial arc introduces a strong constraint on the degree of the central mass concentration in the cluster. For example, in the case of a non-singular mass distribution (finite core) we expect a radially stretched image. This is clearly seen in the case of a circular symmetric lens (Fig. 2). When the source approaches the radial caustics, two images approach each other across a radial critical line along the radial direction and merge into a radially stretched single image. If the density distribution of the lensing object in the central region can be approximated by $\rho \propto r^{-\gamma}$ and $\gamma < 2$, the gravitational potential and the refractive index are finite at the centre of the lens. Hence, the gravitational delay is finite, and a light ray can find its way through the centre of the lens. On the other hand, if $\gamma \geq 2$, the gravitational potential is singular (e.g. $\phi(\vec{r}) \rightarrow -\infty$ when $|\vec{r}| \rightarrow 0$) and the gravitational delay becomes infinite at the centre. Therefore, a light ray which passes near the centre never arrives to the observer. For example, a point mass lens and a singular isothermal sphere do not have radial caustics and will produce two multiple image.^{8) - 14)}

Fig. 3. The caustics and critical lines of an elliptical lens. Left and right panels describe the caustics in the source plane and the critical lines in the image plane, respectively. Four cusp caustics appear at the corners of diamond caustics. The other parts of the caustics are folds. The appearance of the images corresponding to each source position are also shown. The minor axis of the elliptical lens potential is the vertical direction. The ellipticity of the lens potential is larger in the case shown in bottom figures than in the others. Naked cusps appear. When a source lies on a naked cusp, one highly magnified merged image appears without any additional images.

On the other hand, the NFW density profile may have a radial arc¹⁸⁾ since it has $\gamma = 1$ in the central region. It has been sometimes said that the detection of a radial arc is evidence of the finite core radius of the cluster mass distribution.¹¹⁾ However, the only conclusion that can be drawn from the detection of the radial arc is that the density profile of the cluster central region is flatter than $\rho \propto r^{-2}$, e.g. $\gamma < 2$.

Fig. 4. The time delay surface for a circular lens with $\beta = 0$ (left panel) and $\beta \neq 0$ (right panel), where the source position is shifted to negative y -direction. A contour line corresponding to the same height as a saddle point of the time delay surface is also drawn. Each stationary point is named according to their second derivatives: H(high), S(saddle) and L(low) denote the local maximum, the saddle and the local minimum points, respectively. The isochrone appearing in the right panel is named “limaçon”.

The time-delay surface helps us to visualize image configurations for the complex lens model. As we can see from Eq. (2.55), the geometrical delay surface is a concave paraboloid, and the gravitational delay adds a bump to the paraboloid. For a circular symmetric lens with a finite core radius and a perfect alignment source-lens-observer (Fig. 4), $\beta = 0$, and the time-delay surface will display one maximum (H) and one circle as minimum (L). The circle L corresponds to the Einstein ring. For small but finite values of β , the Einstein ring disrupts into one saddle point (S) and one minimum. The total number of the stationary points (hence the number of images) is 3. The total parity of each stationary point is even for H and L images, and odd for S image. If we increase β , H and S will merge (at the critical line) along the radial direction forming the radial arc, and then disappear, and only the L image remains. Note that if the central potential depth is infinite, there is no maximum H and no radial arc can exist. For an elliptical potential and in the perfect alignment case, the ring L disrupts into two Ss (along the major axis of the potential) and two Ls

Fig. 5. The time delay surface for an elliptical lens with $\vec{\beta} = \vec{0}$ (top left panel) and $\beta_x > 0$ ($\beta_y = 0$) (top right and bottom panels). Contour lines corresponding to the same height as a saddle point of the time delay surface and the name of each stationary point are also indicated. In the top two panels, two saddle points appear. Shifting the source position further from the top right panel, two Ls and one S merge into one L, and one obtains the case described by bottom panel. The top right panel has both a limaçon and a lemniscate as isochrones.

(along the minor axis of the potential), because the gradient of the effective lensing potential is different along major and minor axes (Fig. 5). First we consider the case in which a cusp lies inside of the radial caustic. If we shift the source position from perfect alignment along the major axis, two Ls and one S will move closer along a curved trajectory tangential to the lens potential contour and merge, forming a tangential arc. The position of the source at this stage lies at the cusp caustics. If we further shift the source position, the merged image converges into a single L image, and H and S approach along the radial direction and merge into one radial arc, where the source is on the radial caustics. Further outward shifting of the source position causes H and S to disappear, and only the L image remains.

In the case of a naked cusp, first H and S approach along the radial direction and merge into one radial arc, where the source is on the radial caustic, and finally they disappear if we shift the source position from the perfect alignment along the major axis. If we further shift the source position, two Ls and one S become closer and merge, forming a tangential arc. The position of the source at this stage lies at the naked cusp caustics. The elliptical lens can have five or three or one images, and the total number of images always changes by ± 2 when the source crosses a caustic.

In the case of an elliptical lens, one can see another type of important caustic for cluster lensing, that is lips caustics (Fig. 6). We start with the perfect alignment case (Fig. 5). As decreasing the depth of the effective lensing potential, a gradient along the major axis is getting flatter. Finally, two Ss disappear and a central H changes into S. Such caustics are called ‘lips caustics’ because of their shape.¹⁰⁾ The time delay surface and shape of the lips caustics are drawn in Fig. 6. If an extended source fills in the lips caustics, one S and two L images merge into one straight arc. If we further decrease the depth of the effective lensing potential, one S and two Ls merge and disappear, and only one L remains. Since the Laplacian of the time-delay potential reads

$$\Delta t(\vec{\theta}) \propto 2 - \Delta\psi(\vec{\theta}) = 2(1 - \kappa(\vec{\theta})), \quad (2.56)$$

the condition of the maximum point, $\Delta t(\vec{\theta}) < 0$, reads $\kappa(\vec{\theta}) > 1$. Therefore, to have an H image, the surface mass density of the lens must be super critical, and the lens must be super critical for the circular symmetric lens to be able to have strong lensing events and for the elliptical lens to have five images. However, in the case of lips caustics, there is no H, and the lens does not have to be super critical. These diagnostics of the lips shows that the lips caustics appear when the surface mass density of the lens is marginally critical.

The beak-to-beak catastrophe is another example of a marginally critical lens.¹⁰⁾ It is formed of two marginally critical lenses close to each other in the same lens plane. In Fig. 7 the behavior of time delay surfaces for the observer at the middle of two circular lenses in the case that the strengths of two equal lenses are similar, is shown. Decreasing the strength of the lens (that is, decreasing the absolute value of the amplitude of the effective lensing potential) corresponds to putting the source at lower redshift for a fixed lens mass distribution and fixed cosmological parameters. In the case shown in Fig. 7, two L images and one S image appear along the line perpendicular to the line across the two lenses when the source is placed in the

Fig. 6. The lips caustic. The time delay surface for the marginally critical elliptical lens with $\beta = 0$ is shown in the top panel. The major axis of the elliptical lens potential is the x -direction. The bottom left and right panels show the caustic and critical line in this case, respectively. This caustic is called a “lips caustic” because of its shape. The appearance of the images corresponding to each source position are also shown. If the central source size is larger and touches the fold caustic line, three multiply lensed images merge into one straight arc. Even if the source appears on the cusp, the curvature radius of the arc is large, and a nearly straight arc is obtained.

middle of the two lenses. When decreasing the strength of the lenses, two Ls and one S approach and merges, and only one L image remains. The time-delay surface and caustic for this case are shown in Fig. 7. These are termed a ‘beak-to-beak caustic.’ Both lips caustics and beak-to-beak caustics can form straight arcs.^{28), 29)} Lips and beak-to-beaks are not listed as elementary catastrophes. The reason for this is that these are the cross sections by the source plane of the cusp ridges associated with any of the elementary catastrophes in a control space of greater than three dimensions. This situation is illustrated well by Fig. 6.12 in Schneider, Ehlers and Falco.¹⁰⁾

As mentioned at the beginning of this section, three more higher order elementary catastrophes appear, but they always are a combination of cups and folds. Readers can consult the textbook by Schneider, Ehlers and Falco¹⁰⁾ with regard to the application of the higher order catastrophe for the lensing.

Fig. 7. The beak-to-beak caustic. Two critical circular lenses are put on the same lens plane with a small separation. The left top and left middle panels are caustics, and the right ones are critical lines, respectively. The strengths of the lenses are weaker; that is, the source is closer to the lens in the case shown in the top panels. As the source gets closer to the lens, two fold caustic lines appearing in the central region merge and finally disappear (changes from the middle panel to the top panel). The caustics shown in the top panel are called “beak-to-beak” caustics, owing to their shape. The appearance of the images corresponding to each source position are also shown. A highly stretched straight arc is obtained when a source exists at the middle of two lenses. The time delay surfaces and their isochrones for the lens system corresponding to the middle panel are shown in the bottom panels. The left panel is shown for the case when the source, the observer and the middle point of the two lenses are aligned. The case in which the source position is slightly shifted toward the centre of one of the lenses is shown in the right panel.

2.3.1. The strong lensing cross section

For statistical studies of strong lensing events, it is important to compute the lensing cross-section: the probability to observe the image with a magnification larger than a threshold value μ . The computation of the cross-section near fold caustics⁸⁾ gives a good first order approximation of the total cross section. Indeed, most of caustics are folds, and the contribution to the total cross section from a cusp is generally negligible, since they are points. Without loss of generality, the origin of the coordinate system in the source plane can be put on a fold caustic, and the direction of the x and y coordinates can be defined as tangential and perpendicular to the fold caustic, respectively. As long as we are interested in a local estimate, the x -coordinate can be approximated as the caustic line, and the magnification then only depends on the y -coordinate, the distance to the caustic line.

Thus, the cross section near the fold caustics is given by

$$\sigma(\geq \mu) = \oint \int_0^{\beta_y(\mu)} D_s^2 d\beta_x d\beta_y, \quad (2.57)$$

where $\beta_y(\mu)$ is the position where the magnification reaches μ and the integral over β_x is taken along the fold caustic. This equation can be easily rewritten as

$$\sigma(\geq \mu) = \oint \int_0^{\theta_y(\mu)} D_s^2 H(\vec{\theta}) d\theta_x d\theta_y, \quad (2.58)$$

where we have used the fact that the caustic line is mapped onto the critical line. To avoid double counting the area, we integrate only on one side of the critical line, although two images with approximately the same magnification appear in both sides of the critical lines. Since the magnification is infinite at the critical line, the Hessian $H(\vec{0})$ is zero on the critical line. Thus the derivatives of the Hessian along the critical line are also null, in particular, $\partial H(\vec{0})/\partial\theta_x = 0$. Therefore, the Taylor expansion of the Hessian around the critical line is

$$H(\vec{\theta}) = \frac{\partial H(\vec{0})}{\partial\theta_y} \theta_y. \quad (2.59)$$

Then $\theta_y(\mu)$ is defined by μ as

$$\mu = H(\theta_y(\mu))^{-1} = \left(\left| \frac{\partial H(\vec{0})}{\partial\theta_y} \theta_y(\mu) \right| \right)^{-1}. \quad (2.60)$$

Finally we obtain

$$\sigma(\geq \mu) = \frac{1}{2\mu^2} D_s^2 \oint \frac{d\theta_{\parallel}}{|\nabla_{\perp} H|_{H=0}}, \quad (2.61)$$

where $d\theta_{\parallel}$ is the length element along the critical line and $|\nabla_{\perp} H|_{H=0}$ is the gradient of the Hessian in the direction of the perpendicular to the critical line evaluated on the critical line, and to first order it does not depend on μ . We thus conclude that the total cross section to observe lensed images with magnification larger than μ is proportional to μ^{-2} .

§3. Constraining the mass distribution of clusters

3.1. Modelling the mass distribution with strong lensing

Strong lensing events, such as GLAs and multiply imaged arcs (out-standing example is shown in Fig. 8), constitute a powerful tool to constrain the mass distribution of cluster cores. As we have shown in the previous section, the simplest way of estimating the mass of a cluster with strong lensing events is assuming circular symmetry for the lens and to use Eq. (2.19), where the Einstein radius θ_E is estimated from the position or curvature of the arc or from the distance between multiple images. Such an estimate is, however, *very rough* and can easily over or underestimate the effective projected mass in the core.

More accurate modelling of the cluster mass distributions are based on multiple images. The idea here is to optimize the cluster mass model in order to reproduce the observed sets of multiple images within the observational uncertainty. A χ^2 can be defined by the quadratic sum of the difference of the central positions of each image mapped onto the source plane divided by the observational uncertainty scaled by the lens mapping. Alternatively, it can be defined as the quadratic sum of the difference between the actual observed images and the images of a fiducial source. The elongation and orientation of each image can in principle be added to the optimization procedure. However, due to the relatively large observational uncertainty compared to the image position, they generally impose a loose constraint. Since the number of available observational constraints is not large, the number of parameters describing the cluster mass distribution should be of the same order as the number of constraints. For this reason, the mass model is often described by a linear sum of mass clumps described analytically. One of the first best known examples of a cluster mass model is the model of A370 by Kneib, Mellier, Fort and Mathez.³⁰⁾ Their model is very simple in the sense that it has only two mass clumps centred on the two giant ellipticals of that cluster, and was constrained by the giant arc (a triple image) and another triple image, B2-B3-B4. From their model they could predict the redshift for the source of B2 to be $z \sim 0.865$. Figure 9 shows the central part of A370 seen with *HST*/WFPC2 in F675W, with the improved mass distribution model by Bézecourt

Fig. 8. The *HST*/WFPC2 image of CL0024+1654 at $z = 0.39$. One can clearly see that one galaxy is multiply imaged, 7 images in this case. The change of the parity and blue nature of the lensed images can be observed.

Fig. 9. The central part of A370 taken by *HST*/WFPC2 image in F675W the top panel.³¹⁾ Overlaid is the mass distribution (black thin lines). The most important arclets and multiple images are colored. The radial arc can be observed in the south clump. The contour map of the X-ray emission obtained by *ROSAT*/HRI is shown in the bottom panel. This is taken from Hashimoto-dani.⁴⁴⁾ The crosses indicate the positions of the two cD galaxies. There is a small cave close to the northern cD. North is up in both figures.

et al.³¹⁾ that extends the former model including cluster galaxies (following the prescriptions of Kneib et al.³²⁾ The latest model of A370 is based on two sets of double images and four sets of triple images with a spectroscopic redshift for two of them. The fact that the source redshift of B2 was first predicted by Kneib et al.³⁰⁾ and then confirmed spectroscopically by Bézecourt et al.,³¹⁾ strengthens support for the reliability of the model.

Cluster-lenses mass models have been considerably improved with the refurbishment of the Hubble Space Telescope (HST). Indeed, the high image-resolution of the *HST*/WFPC2 camera on a reasonably wide field makes it a unique instrument to probe the mass distribution of cluster cores. As was first shown by Kneib et al.,³²⁾ thanks to the identification of a larger number of multiple images, it is possible to constrain the mass distribution on the scale from ~ 500 kpc down to the galaxy scale ~ 10 kpc. Strong lensing events *do* constrain the mass distribution of the cluster core, and more specially the mass-to-light ratio of cluster galaxies. Furthermore, by measuring the deviation of the shear field from the prediction of the cluster potential which is constrained by strong lensing events, the amplitude of the perturbations due to the cluster member galaxies can be evaluated.³³⁾ Therefore, the mass-to-light ratio of the cluster member galaxies can be constrained. Such an approach combined with the weak (galaxy-galaxy) lensing approach can measure even more accurately the masses of galaxies.^{33), 34)}

3.2. Comparison with X-ray results

Clusters of galaxies contain huge amounts of hot gas, which emit X-ray through bremsstrahlung. This hot gas constitutes the intra-cluster medium (ICM). Since the sound crossing time of the ICM through the cluster core is $\sim 10^8$ yr and generally is much less than the age of the cluster (\sim several $\times 10^9$ yr), the ICM could be described well by hydrostatic equilibrium. Therefore, if the gas density distribution and the hot gas temperature distribution are measured, the mass distribution of the cluster can be obtained by solving the equation of hydrostatic equilibrium. The *ROSAT*/HRI³⁵⁾ had a good spatial resolution in 0.1–2keV and has provided precise information on the distribution of the ICM. The *ASCA*³⁷⁾ satellite has a good spectral resolution in the 0.5–10keV band and is the first instrument able to measure the ICM temperature in the distant lensing cluster (despite a poor spatial resolution). We were very lucky to have both complementary X-ray satellite past five years, while the lensing study of the cluster mass distribution was emerging as a new powerful tool to constrain cluster mass distributions. Lensing and X-ray studies of the cluster mass distributions are complementary. While X-ray studies of cluster mass distributions require some assumptions on the thermal and dynamical state of the ICM, lensing directly maps the surface mass density of the cluster, regardless of its dynamical and thermal state. Therefore, lensing studies of cluster mass distributions are more reliable than X-rays *if* sufficiently accurate lensing constraints are available. Comparison of the two results provides information on the thermal and dynamical states of clusters. Such a comparison may also shed new light on the formation and evolution of clusters which tightly links them to modern cosmological interests.

Peebles³⁸⁾ wrote in 1993, “[...] we are going to extrapolate the physics that

is known to be successful until it is seen to fail. [...] the extrapolation out in space and back in time is by no means without empirical support. [...] gravitational lensing of background galaxies by the mass concentrations in clusters of galaxies, as analyzed in general relativity theory, is consistent with the masses derived from the motions of the galaxies and from the plasma pressure within the clusters. The relevant length scale here — the impact parameter at the center — is ten orders of magnitude larger than that of the precision tests of general relativity in the Solar System and in binary pulsar systems, a remarkable extrapolation.”

However, soon after the publication of Peebles’ textbook, it was claimed that the mass in the cluster core region estimated from strong lensing effects is systematically a few times larger than the mass estimated by X-ray observations under the assumption of the hydrostatic equilibrium of the ICM.^{39) - 43)} The simple comparison discussed in these papers has created a great deal of excitement and discussion, in order to try to explain such discrepancy. Hashimoto-dani⁴⁴⁾ showed that the discrepancy between the lensing and X-ray approaches seems to be systematic on a large sample of 30 distant cluster lenses (Fig. 10). Such analyses on such large samples was first made by Wu and Fang,⁴¹⁾ but their X-ray mass estimates were not an accurate, since they were not using *ROSAT/HRI* and *ASCA* data. Allen⁴⁵⁾ also analyzed the *ROSAT/HRI* and *ASCA* data of 13 distant cluster lenses and obtained the first reliable mass estimations based on X-ray observations, and has made the first robust confirmation of the existence of the systematic discrepancy.

Fig. 10. The comparison of the cluster mass obtained by X-ray observations with those obtained by modelling of strong lensing events. The lensing masses are quoted from the literature, mostly from Wu and Fang.⁴¹⁾ This figure is quoted from Hashimoto-dani.⁴⁴⁾

3.3. *Understanding the mass discrepancy*

In this section we introduce ideas proposed to solve the mass discrepancy. We also attempt to discuss the best current understanding of the problem.

3.3.1. Non-thermal pressure

Loeb and Mao³⁹⁾ proposed that non-thermal pressure induced by equipartition turbulent and magnetic pressure plays a crucial role in supporting the ICM against the cluster gravitational pull. Therefore, if one neglects the contribution of these

non-thermal pressures, one could easily underestimate the gravitational mass of the cluster from the ICM distribution by a factor of 2–3. They concluded that the observed high Faraday rotation measures (hereafter RM) in the directions of radio lobes in several (low- z) clusters would be consistent with the required equipartition magnetic field needed in lensing clusters to resolve the discrepancy. However, Makino⁴⁶⁾ pointed out that the magnetic field strength estimated from the RM in the direction of background radio sources is an order of magnitude less than the equipartition magnetic field strength. He argued that the extremely high RM obtained in the direction of the radio lobe is likely to be intrinsic to the radio lobe but not to the ICM. The magnetic field strength in cluster lenses is undetermined at present. It is, however, constrained by hard X-ray and radio observations. Indeed, extended radio halo caused by synchrotron radiation has been detected from several nearby clusters.⁴⁷⁾ The relativistic electrons in the cluster, which constitute the source of the synchrotron radiation, produce a hard X-ray tail in the cluster X-ray spectrum by inverse Compton scattering of the cosmic microwave background radiation.⁴⁸⁾ It is expected that the next generation of X-ray satellites (*Astro-E*) will judge the possibility of the equipartition magnetic field in the ICM by measuring the hard X-ray tail.

3.3.2. Elongation of the cluster and 3D mass distribution

Loeb and Mao³⁹⁾ pointed out that the cluster elongation along the line of sight is not a plausible explanation since it would require a large axial ratio that would cause a dynamical instability.²²⁾ Furthermore, it is very unlikely that all the lensing clusters are elongated along the line of sight by accident. However, the possibility of the superposition of several clusters along the line of sight could easily explain the discrepancy observed for some optically selected lensing cluster. For example, the deep wide field redshift survey of Cl0024+1654^{49), 50)} seems to favor the existence of the superposition of two close-by clusters.

3.3.3. Cooling flow

Clusters of galaxies are categorized into two groups according to the nature of the distribution of the ICM in the cluster core. The clusters in which the X-ray emission has a prominent central peak that coincides with the center of a bright elliptical galaxy is called *XD*. Clusters in which the X-ray emission is dispersed and does not exhibit a clear coincidence between the X-ray peak and the bright galaxy center is called *non-XD*.⁵¹⁾ The XD clusters are believed to harbour a cooling flow.⁵²⁾

The multi-phase nature of the ICM in the central part of clusters due to cooling flow has been considered as a possible source of the underestimation of the X-ray cluster mass.^{45), 53)} Allen⁴⁵⁾ studied X-ray data of 13 lensing clusters of galaxies and broke his sample into three groups, on their central cooling time: cooling flows, non-cooling flows, and intermediate samples. He showed that the mass discrepancy is significantly reduced for cooling flow samples by applying the cooling flow model to the spectral fitting. If the cooler components induced by cooling flow exists, the temperature of the hottest component should become higher by a factor of 2–3 than the temperature obtained by a single phase model fitting of the observed emissivity-weighted temperature. Since the hydrostatic mass depends linearly on the

temperature of the hottest phase, it increases the X-ray mass. He also noticed that the centre of the X-ray emission is significantly shifted from the centres of curvature of the lensed arc for the non-cooling flow sample. Therefore, these clusters may not be in dynamical equilibrium and probably are post-mergers. However, several arguments do not support this idea. *ASCA* data of nearby XD clusters are fitted well by a two-temperature phase model in the core and with a single phase model in the outer region.⁵⁴⁾ The hotter phase stays isothermal throughout the cluster, and the weighted averaged temperature throughout the cluster is not so much different from the temperature of the hotter phase; this seems to be contradictory to Allen's⁴⁵⁾ analysis. The distant cluster RXJ1347-1145 is the most X-ray luminous cluster ever discovered and is thought to have an extremely massive cooling flow, according to Allen.⁴⁵⁾ Recently a radial profile of the Sunyaev-Zel'dovich (hereafter SZ) increment was measured by *JCMT/SCUBA*⁵⁵⁾ for this cluster. It was shown that the combined fitting⁵⁶⁾ to the X-ray spectrum obtained by *ASCA* and to the SZ radial profile puts a strong constraint on the strength of the possible cooling flow and leads us to reject the massive cooling flow model proposed by Allen.⁴⁵⁾

Clearly, deeper insight here is needed to improve our knowledge on the cooling flow model. The next generation of X-ray satellites, like *AXAF/XMM* with their spatially high-resolution temperature measurement (of cluster-lenses) and *Astro-E* with its high resolution X-ray line spectroscopy (of nearby cooling flow candidate clusters), and on-going (e.g. *JCMT/SCUBA*) and future projects (e.g. *LSA/MMA*, *LMSA*) of mm and submm observations of SZ and dust emission from clusters,⁵⁷⁾ will soon help us in understanding the physical properties of the ICM in a cooling flow cluster.

3.3.4. ICM not in dynamical equilibrium

Allen⁴⁵⁾ also suggests that for non-cooling flow cluster, the main reason for the discrepancy is that these clusters are not in dynamical equilibrium, as they are post-mergers. The evidence given to support this idea (see also Hashimoto⁴⁴⁾) is that the centre of the X-ray emission is significantly shifted from the centres of curvature of the lensed arc. Such a possibility was first proposed by Kneib et al.,⁵⁸⁾ in their detailed mass distribution model of A2218 based on lensing data and compared with the *ROSAT/HRI* X-ray map. The lensing model predicts a bimodal distribution centered on the two brightest cluster galaxies. The distribution of the X-ray emitting gas is, however, not consistent with the lensing mass model: the X-ray bright core is elongated perpendicular to the elongation of the lens model, with a shift in the position. Moreover, there is no secondary peak in the X-ray emission associated with the secondary clump inferred from the lens model. Thus, they suggested that the ICM in A2218 is highly disturbed by the passage of a subcluster, and the ICM is no longer in hydrostatic equilibrium in the cluster core.

This possibility is also supported by other evidence. The left-hand side of Eq. (2.47) is $(830\text{km/sec})^2 = 6.9 \times 10^{15}\text{cm}^2/\text{sec}^2$ for the main clump model presented in Kneib et al.⁵⁸⁾ The best fitting values to the X-ray data yields $(\beta/0.62)(k_B T/7.04\text{keV}) = 6.6 \times 10^{15}\text{cm}^2/\text{sec}^2$ for the right-hand side of Eq. (2.47). These two values are consistent within X-ray measurement errors for temperature $7.04 \pm 0.07\text{keV}$ ⁵⁹⁾ and

for slope parameter of X-ray surface brightness $\beta = 0.62^{+0.13}_{-0.09}$ ⁴⁴⁾ where errors are 90% one parameter errors. The main discrepancy in this cluster can be explained by the large X-ray core radius of $53''$,^{60), 61)} compared to the value in the lensing model, $\sim 20''$. A simple check of this can be done in the following way. Inserting $\theta_c = 53''$, $\theta_E = 23''$ and $z_s = 2.6$ into Eq. (2.36) yields $k_B T = 17\text{keV}$, while $\theta_c = 20''$ yields $k_B T = 9.5\text{keV}$, which is close to the measured temperature. If the post-merger causes the cluster central gas to disperse and to thus forces it away from equilibrium, but allows for the dark matter distribution to remain centrally concentrated (as suggested by lensing), one should use a core radius of $\sim 50 - 100 h_{50}^{-1}\text{kpc}$ (about $20''$) for the dark matter distribution (which is the typical X-ray core radius for an XD cluster). Then, assuming that the gas distribution at the cluster outskirts is in hydrostatic equilibrium, where the observed β value and the temperature are measured, the mass discrepancy problem for A2218 is solved. The last assumption may be safely applied, since the mass of the subclump supposed to have collided is much smaller than the mass of the main clump.⁵⁸⁾

3.3.5. Effects of complex mass distribution

Recent studies have revealed other plausible possibilities to reconcile the discrepancy. The main reason here is overestimation in the lensing mass determinations. By definition, a large number of galaxies populates the cluster core. Therefore, we cannot neglect the contribution of their stellar mass and their dark halos. With such complex models, the total mass needed to produce arcs is significantly decreased compared to smoothed and symmetric models.

Fig. 11. The central part of cluster A2390 seen with *HST*/WFPC2/F814W. A-B-C is a straight arc. It is in fact composed of two objects: B-C at $z = 0.913$ and A at $z = 1.03$. The objects H3a-b and H5a-b are two sets of multiple images with $z = 4.06$.¹¹¹⁾

For example, Abell 2390 has a “straight” arc.²⁸⁾ It requires a special geometry

for the mass distribution of the lensing object and imposes a strong constraint on the cluster mass distribution (Fig. 11). Pierre et al.⁶²⁾ presented a detailed analysis of the *ROSAT*/HRI image and found an extended local sub-peak of X-ray emission which might be associated with the existence of a dark matter clump. This clump would act as a perturber, just as predicted by Pelló et al.,²⁸⁾ to reproduce the straight arc. In fact Pierre et al.⁶²⁾ successfully constructed a lens model of A2390 defined by two mass clumps. Böhringer et al.⁶³⁾ measured the temperature of this cluster and studied its X-ray data, which exhibits a very smooth, centrally peaked X-ray emission, and evidence of massive undisturbed cooling flow, indicating that the ICM is in hydrostatic equilibrium in the cluster potential. They showed that the X-ray mass estimation assuming that the cooling flow has little effect on the temperature measurement agrees well with the lensing mass inferred by Pierre et al.⁶²⁾ If the lensing mass of this cluster is estimated with the formula for the circular symmetric lens, the estimated mass is several times larger than the X-ray mass. These results indicate that the introduction of a small asymmetry in the mass distribution of the cluster core can substantially reduce the lensing mass compared to the circular symmetric approximation.

Hattori et al.⁶⁴⁾ showed that in the distant cooling flow cluster CL2236-04, lensing and X-ray masses agree if the lensing mass model includes a second clump of mass centered on the second brightest member (Fig. 12). This successful lens model was first proposed by Kneib et al.⁶⁵⁾ prior to any X-ray observations.

Similarly, Hashimoto et al.⁶⁷⁾ have shown that there is no discrepancy if a secondary potential due to the bright cluster galaxy near the arcs of MS0302.7+1658 and MS1621.5+2640 is included in the lensing model. If the contributions of the secondary clump are not taken into account, the X-ray mass of the clusters are a factor of 2–4 less than the required mass to explain the arc positions in these two clusters. Therefore, the introduction of the secondary galaxy potential is essential.

In the case of the above mentioned clusters, the nature of the galaxy potentials are constrained consistently with their optical properties. The strong lensing in CL2236-04 and MS0302.7+1658 is an example of marginal lensing (lips in CL2236-04 and beak-to-beak in MS0302.7+1658).

Fig. 12. The V+R image of CL2236-04 at $z = 0.55$ taken by ESO 3.6m⁶⁶⁾ superposed on the X-ray image obtained by *ROSAT*/HRI.⁶⁴⁾ The straight arc at $z = 1.16$, as bright as the bright cluster member galaxies, can be observed at the north of the cluster core. A bright cluster member galaxy exists close to the arc.

3.4. *A closer look at individual cases*

It seems that the discrepancy could be explained by different arguments. To get a better feeling of the current limitation on the data, we now describe in detail some peculiar cases.

3.4.1. MS1621.5+2640

The situation in MS1621.5+2640 is typically a barely constrained cluster lens. The observed arc A1 configuration can be reproduced by qualitatively different mass distribution models.⁶⁷⁾ The first model assumes that the ICM is isothermal and in hydrostatic equilibrium. The second model assumes that the dark matter distribution has a small core radius of ~ 50 kpc but is much smaller than the X-ray core radius of MS1621 ($r_c^X = 256$ kpc). The last possibility was considered to take into account a possibility similar to A2218. As pointed out by Moris et al.,⁶⁸⁾ the large core radius and irregular morphology of MS1621.5+2640 may be a signature of a disturbed distribution of the ICM due to merger.

Arc A1 can be explained by both models if a secondary galaxy contribution is taken into account. However, we cannot distinguish between models at this moment — mainly due to a lack of lensing constraints. Deeper lensing/X-ray observations will be important to understand the discrepancy.

3.4.2. RXJ1347.5-1145

The origin and history of the discrepancy for RXJ1347.5-1145 is somewhat different from others. Schindler et al.⁷⁰⁾ found two arcs in this field. Schindler et al.⁷²⁾ made a lensing mass estimation assuming that they are multiple images, and found that the lensing mass is a factor of three larger than that expected from X-ray observations. However, it is now clear that they are single images of different background galaxies, according to their color difference.⁷¹⁾ Therefore, the mass estimate made by assuming that the arc position is the same as the Einstein ring radius is not valid (and this is the case for other clusters). Fischer and Tyson⁷¹⁾ measured a weak lensing shear field and found that the mass obtained by a weak lensing mass reconstruction is a factor of 2 larger than that expected from X-ray observations.⁷²⁾ However, as they do not have any multiple images, it is very difficult to believe an absolute mass estimate from weak shear estimates, as this will depend on the assumed redshift distribution of the background galaxies as well as the correction factor applied to compensate for the seeing effect. For example, if the mean source redshift of the shear field measured by Fischer and Tyson⁷¹⁾ through RXJ1347.5-1145 is as large as 1 (and not ~ 0.65 , as they assumed) the required weak-shear mass is reduced by a factor of 2, and both the lensing and X-ray mass estimation provide consistent results. A photometric estimate of the source redshift may in the near future address such problems in more detail, especially with the new 8–10m class telescope, which offers deep high quality images in relatively short exposures.

3.4.3. A370

The cluster A370 is one of the best modeled lensing clusters.^{30), 31)} Ota, Mitsuda and Fukazawa⁴²⁾ found a factor of 2 discrepancy in the cluster central mass estimation between X-ray and strong lensing. However, the assumed cluster center includes

very large error because of the poor *ASCA* position determination accuracy ($\sim 1'$). Hashimoto⁴⁴⁾ analyzed *ROSAT*/*HRI* data and obtained interesting results (Fig. 9). The X-ray emission is peaked at the center of the southern cD galaxy (see Fig. 9). However, there is no X-ray peak associated with the northern cD, although the velocity dispersion and the core radius of the northern clump are similar to those of the southern clump in the lens model.³¹⁾ The existence of the northern mass clump has also been confirmed by the weak lensing mass reconstruction using the *HST*/*WFPC2* image,⁷⁾ been therefore making its existence certain. Hashimoto⁴⁴⁾ revised the results of the *ASCA* temperature. It can be safely assumed that the temperature measured by *ASCA* is the temperature of the gas associated with the southern clump only. Checking the left- and right-hand sides of Eq. (2.47), they derived β and the temperature, and found them to be consistent with the velocity dispersion of the lens model.³¹⁾ The X-ray core radius of the southern clump is also consistent with the lens model. Therefore, for the southern clump, X-ray results are consistent with the mass distribution of the southern clump predicted by lens modelling.

Thus, the problem now, is to explain why no X-ray emission is detected in the northern clump. Is this due to merger? May the gas around the northern clump and the southern clump just have merged? But then why did the southern clump not suffer from the merging? It is likely that A370 is the superposition of two clusters with slightly different redshifts, as suggested by their velocity histogramme. However, this is not a fully satisfactory explanation, as very few X-rays are detected in the Northern clump.

Spatially resolved X-ray spectroscopy with *AXAF* and *XMM* observations and a deep wide field spectroscopy survey similar to the C10024+1654 survey will provide exciting new insight for understanding cluster formation.

3.4.4. Is there really a discrepancy?

It is now clear that comparison between strong lensing and the X-ray mass must be done carefully from cluster to cluster, based on the detailed X-ray image and galaxy distributions. However, we must note that, except for a few well studied clusters as introduced in this section, the lensing studies are sometimes not done very accurately — especially when they estimate the mass from the Einstein radius. Since the measurement of the mass of the cluster with strong lensing events is based on model fitting, if the model introduced is not motivated physically, it may lead to a large systematical error in mass estimation.

Further work on the mass discrepancy between X-ray and lensing studies should consider seriously the complexity of the mass distribution (This is in particular true for the lensing estimate, but it also applies to X-ray analysis.) before reaching a hasty conclusion on an unlikely mass discrepancy.

3.5. Implications

In this section, we summarize what we have learned from strong lensing studies of the cluster mass.

3.5.1. Radial arcs and the very central mass profile

As explained in §2, the radial arcs impose a strong constraint on the degree of central mass concentration in the cluster. Clusters with a radial arc are listed in Table I. A good example of a radial arc is shown in Fig. 13. Radial arcs can only be seen on the HST images for A370/MS0440/AC118, as they are very thin! The existence of the radial arcs in these systems favors a central surface mass density distribution flatter than $\propto \theta^{-1}$ (a mass density distribution flatter than $\propto r^{-2}$). The thinness of the radial arcs would indicate a relatively cuspy mass profile; that is $0.5 < \delta < 1$, where $\Sigma \propto \theta^{-\delta}$. The expected slope of the surface mass density is steeper than that of NFW. This may suggest that the radial mass density profile of the cluster central region is steeper than r^{-1} , as indicated by the higher resolution simulation using GRAPE,⁽⁷⁷⁾ which has a higher resolution than NFW's simulation. However, the central giant elliptical certainly has influence on the width of radial arcs. Therefore, the detailed quantification of the tangential deformation rate of the radial arcs are very important. Resolving the width, measuring the redshift and the velocity dispersion of the source galaxies of radial arcs, and measuring the velocity dispersion profile of the central elliptical galaxy will be key observations of the 10m class telescopes, such as Keck, SUBARU, VLT, Gemini and in the moderate future NGST.

Table I. List of detected radial arcs. The first column contains the names of the clusters and radial arcs. The paper in which the radial arc was first reported is cited. Since the radial arcs are elongated along the radial direction by about a few arcsec, the distance to nearby cD is measured from the approximate arc center and is shown in the second column. The third column gives the redshift of the clusters. None have a spectroscopic redshift yet. The last column is the model prediction of the arc redshift.

cluster (arc name)	dist to cD	z_d	z_{pred}
MS2137-23 (A1) ⁽⁷³⁾	$\sim 5''$	0.313	-
A370 (R) ⁽¹⁰⁵⁾	$\sim 8.''4$	0.37	1.3 ± 0.2 ⁽¹⁰⁵⁾
MS0440+02 (A16) ⁽⁷⁴⁾	$\sim 6''$	0.19	-
MS0440+02 (A17) ⁽⁷⁴⁾	$\sim 6''$	0.19	-
AC114 (A4-A5) ⁽³³⁾	$\sim 2.''7$	0.31	1.76 ± 0.15 ⁽³³⁾
AC118 ⁽⁷⁵⁾	$\sim 5''$	0.33	-
AC118 ⁽⁷⁵⁾	$\sim 5''$	0.33	-
CL0024-1658 ⁽⁷⁵⁾	$\sim 10''$	0.39	-

3.5.2. The cooling flow interpretation

Important implications for the cooling flow model can be extracted from the studies of A2390, CL2236-04 and MS0302.7+1658. These clusters have a high central electron density and a short radiative cooling time and therefore are expected to have cooling flow. Cluster mass estimates from X-ray observations using ASCA data with a single phase model fitting⁽⁶⁴⁾ are consistent with the strong lensing estimate. If the effect of the cooling flow is significant, the temperature of the hottest phase gas in these clusters could be a factor of 2–3 higher than the single phase model fitting results. However, these two clusters are marginal lenses, and the lens models are very sensitive to the total mass, and therefore to the cluster temperature. Increasing the

Fig. 13. The central part of cluster MS2137-23 seen with *HST*/WFPC2/F702W.⁷⁶⁾ A radial arc is clearly seen.

temperature by more than factor of 2 is incompatible with the existence of a straight arc in these clusters. Therefore, even if cooling flow exists in these clusters, the deviation of the hottest phase temperature from the *ASCA* measured temperature must be negligible.

3.5.3. Existence of a universal mass profile

The two models that can explain the observed arc configuration of MS1621.5+2640 have very important but very different cosmological implications. If the hydrostatic model is correct, MS1621.5+2640 has a very large core radius and a low central electron density, respectively a factor of 5 larger and 10 less than those of MS0302.7+1658. MS1621.5+2640 is known to be a non-cooling flow cluster, since its central cooling time is longer than the Hubble time, although the temperature of MS1621.5+2640, $\sim 6.5\text{keV}$, is not much different from that of MS0302.7+1658, $\sim 5\text{keV}$. This indicates that there are large variations in the core radius and the central density of the cluster mass distribution even if the temperature of the clusters have similar values. This fact has been noticed by Fujita and Takahara,⁷⁸⁾ who

examined the fundamental plane of nearby clusters. They concluded that if the ratio of the dark matter density to the gas density at the cluster center is constant in all clusters, the cluster mass distribution cannot be characterized only by its virial mass and redshift; the formation epoch of the cluster and its evolutionary history may also be important parameters. Since Hashimoto et al.⁶⁷⁾ are using lens modelling to estimate the central dark matter density, their results are free of the assumption on the ratio between the dark matter and gas densities. Therefore, the standard Press-Schechter theory⁷⁹⁾ should be used with caution, as it assumes that the cluster is just virialized at the observed redshift when the theoretical prediction of the cluster temperature and luminosity functions are made. Modifications of the standard Press-Schechter theory, which take into account the difference between the formation and observed redshift, are thus crucial for comparing the theoretical predictions with the observed cluster temperature and luminosity functions.^{80)–84)} Nevertheless, if the compact core model is correct, it indicates that the central electron density is not a good representative of the central dark matter density, and the possibility that the clusters have a universal mass density profile, characterized only by its redshift and virial temperature, may then be close to reality.

It is also worth to note that Bartelmann and Steinmetz¹⁴²⁾ claim that the β -model does not provide a good description of the X-ray surface brightness profile of clusters as determined from their N -body-hydrodynamics simulations. They argue that the β -values in the fit depend critically on the background level and that this introduces a significant bias in the mass determination built on β -model fits. Actually for most of the lensing clusters, the central X-ray surface brightness is close to the background level of *ROSAT*/HRI, and the β values obtained, $\beta \sim 0.45 - 0.55$, are systematically somewhat lower than those for nearby clusters, $\beta \sim 0.6 - 0.7$. However, we have seen that the cluster mass distribution models constructed with these relatively small β values are consistent with the cluster mass distribution modeled by the strong lensing observations. Although this result may interpret that the obtained small value of β for the distant lensing clusters represents the real mass distribution well, further X-ray observations with much higher sensitivities and with similar or better spatial resolution than *ROSAT*/HRI, e.g. *AXAF*, *XMM*, are required to clarify the radial profile of clusters in the outskirts.

3.5.4. Extrapolation of general relativity up to the cluster scale

We can now draw important conclusions concerning whether cluster lensing provides empirical support for the extrapolation of general relativity up to the cluster scale. If this extrapolation fails on the cluster scale, then the discrepancy between lensing and X-ray mass estimates should be systematic. However, as we have seen, excellent agreement between these results has already been reported in about half a dozen clusters. Clusters still exhibiting a discrepancy are likely to be understood in an astronomical context when better quality data are in hand to complete a detailed analysis. Therefore, we conclude that the extrapolation of general relativity up to the cluster scale is empirically supported by cluster lensing.

§4. The missing lens problem and very distant clusters

Looking for and studying very distant galaxy clusters, clusters with $z > 1$, are very important because: i) the number density of rich clusters at large redshifts is a very sensitive measure of the mean density of the Universe; ii) high redshift clusters provide important information to understand the formation and evolution of galaxies (e.g. the evolution of the metallicity of the hot intra-cluster medium, morphological evolution, and star formation history in a dense environment).

However, this is a difficult enterprise, as there are yet only a few confirmed very distant galaxy clusters. The first necessary step is to identify very distant clusters by conducting very deep observations. A random search of the sky is not practical since one expects to detect only a very small number of very distant clusters. A possible route to identify high redshift clusters is to search in a dark lenses field, as explained below.

The expression ‘*missing lens problem*’ can be found in the unique textbook on gravitational lensing written by Schneider, Ehlers and Falco.¹⁰⁾ A number of quasar pairs are candidates to be lensed systems. In a high fraction of these systems, either no deflector or only a part of a deflector is clearly identified. The difference between this problem and the usual missing mass problem is that the mass-to-light ratio required to explain the pair of quasars by a gravitational effect is extremely large compared to that of galaxies. A yet unidentified part of lens objects (distinct from a galaxy and/or galaxy clusters), is called a ‘dark lens’. The dark lens search is an attempt to identify dark lens objects as already known objects.⁸⁵⁾ If all ultra-deep multi-wavelength searches fail to find any evidence of galaxies and/or clusters as the lenses, it could lead us to conclude the existence of a yet unknown new type of object which contains barely any luminous matter. Table 2 of Hattori⁸⁶⁾ summarizes such lens candidates. A large fraction of the lens candidates exhibit the missing lens problem. We now discuss two of them, for which mysterious rich clusters of galaxies may play an important role.

4.1. The lens system MG2016+112

Hattori et al.⁸⁷⁾ have discovered a cluster of galaxies at $z = 1$, named AXJ2019+1127, using X-ray observations in the direction of MG2016+112, a confirmed multiple QSO at $z = 3.27$.⁸⁸⁾ When discovered, this cluster was claimed to be a dark cluster because of the lack of an optical counterpart,^{89), 90)} although the existence of a massive cluster has been predicted by theoretical modelling.⁹¹⁾ Recent deep spectroscopic and imaging studies in optical and IR bands unveiled the nature of the dark cluster. Kneib et al.⁹²⁾ spectroscopically found 6 possible member galaxies in this field (Fig. 14). Using deep V , I Keck images, and wide-field K_s NTT images, Benítez et al.⁹³⁾ found a tight red sequence of galaxies which has a slope in good agreement with the model predictions for $z \sim 1$ clusters.⁹⁴⁾ Based on the identified number of member galaxies⁹³⁾ and the mass estimated from the X-ray temperature,⁸⁷⁾ the mass-to-light ratio within an aperture of $0.8h_{50}^{-1}$ Mpc was found to be $M/L_V \sim 110h_{50}$, which is consistent with the mass-to-light ratio found in nearby clusters.⁹⁵⁾ Therefore, it is very likely that a massive cluster of galaxies ex-

Fig. 14. Unveiling the nature of the dark cluster AXJ2019+112. The I-band image of AXJ2019+112 field taken with *NOT* and overlaid X-ray contours taken by *ROSAT/HRI*.⁸⁷⁾ The spectroscopically measured redshifts of galaxies are attached and possible member galaxies of the cluster AXJ2019+112 are marked by “the thick circle.” Although a dozen member galaxies were confirmed by deep Keck imaging studies and photometric studies,⁹³⁾ there is a debate on the interpretation of the *ROSAT/HRI* results.

ists at $z = 1$ in the line-of-sight of MG2016+112. AXJ2019+1127 is one of the most massive clusters known at $z \sim 1$. Furthermore, it is one of the rare high-redshift clusters for which strong lensing events are clearly detected. Thus, it provides a unique opportunity to study the mass distribution in a very high redshift cluster. Benítez et al.⁹³⁾ successfully modeled (with a cluster surface mass density distribution similar to the NFW model) the multiple images of QSO and the extended arc-like image detected in the *HST*/NICMOS image. The cluster mass derived from the lens modelling is also consistent with X-ray results.

It is worth noting that the Einstein ring radius of AXJ2019+112 is about $2''$ ⁸⁹⁾ if the cluster centre coincides with the giant elliptical located at the middle of the triple QSO images, and it is very small compared to clusters at intermediate redshift ($z \sim 0.2 - 0.5$), which are as hot as AXJ2019+112. Therefore, the central surface mass density of AXJ2019+112 is shallower than those cluster lenses with similar temperatures at intermediate redshift. This may be reflecting the situation in which 1) there is a large variation in the central surface mass density from cluster to cluster independent of their redshift, or 2) there is a strong evolution in the central surface mass density. However, it should be emphasized that the interpretation of the *ROSAT*/HRI results of AXJ2019+112 leads to different results.^{87), 93)} Although Benítez et al.⁹³⁾ claimed that there are three X-ray sources in this field, since there are three patches in the X-ray image, it is dangerous to take these as real sources. For example, the early *ROSAT*/HRI image of A370¹¹⁾ exhibited two X-ray peaks coinciding with the centre of the two giant ellipticals. However, as shown in Fig. 9, the most up-to-date X-ray image of A370 (with an exposure time twenty times longer than the previous one) does show only one prominent peak. Clearly, photon statistical errors must be considered seriously before reaching hasty, unjustified conclusions. Therefore, determination of the accurate cluster central position, morphological studies by detecting more than an order of magnitude larger number of X-ray photons, and the accurate measurement of the X-ray temperature of AXJ2019+1127 will be key observations to conduct with future X-ray missions.

4.2. The double quasar Q2345+007

The quasar Q2345+007 has been one of the most mysterious lens candidates of double quasars since its discovery.⁹⁶⁾ In spite of deep and wide field optical searches, the main lens has not yet been identified.⁹⁷⁾ A very faint galaxy was found at the edge of the secondary image, B image, after subtraction of the point spread function of the image.⁹⁸⁾ Since a C IV doublet absorption line ($z = 1.483$)^{99), 100)} was found in the B image, the redshift of the faint galaxy is supposed to be 1.483. However, the expected mass of the galaxy is too small to explain the wide separation of the two images, unless it has an extremely large mass-to-light ratio. A large cluster at $z = 1.49$ was claimed, since both of the two images have metal absorption lines with redshift $z = 1.491$. Bonnet et al.¹⁰¹⁾ reported the detection of a possible lensing cluster from a weak lensing shear field with a strength of $\gamma \sim 0.15$, confirmed by van Waerbeke et al.¹⁰²⁾ and arclet candidates. After this detection, a galaxy cluster candidate was found as an enhancement in the number density of faint galaxies at the right location in the sky predicted by the shear field.^{98), 103)} Pelló et al.¹⁰⁴⁾ made photometric

redshift estimations for the galaxies in the cluster candidate field and found an excess of galaxies at $z \sim 0.75 \pm 0.1$. Assuming the cluster has this redshift, the velocity dispersion required to produce the observed shear pattern should be 790_{-170}^{+115} km/s,¹⁰⁴⁾ which corresponds to a hot gas temperature of $k_{\text{B}}T \sim 4.1_{-1.6}^{+1.3}(\beta/1.0)^{-1}$ keV. The typical value of β (~ 0.66) yields $k_{\text{B}}T \sim 6.2$ keV, which is as hot as CL2236-04 at $z = 0.552$. Therefore, it is expected that the cluster speculated from the lensing and photometric studies is a bright X-ray source. However, non detection of X-ray emissions from the cluster by *ASCA* and *ROSAT*/HRI observations was reported.⁸⁶⁾ This deepened the mystery further.

4.3. Implications

Other than the original interest in the missing lens problem (that is that it indicates the existence of a yet unknown new type of dark objects in the universe), it is likely that the dark lens search is an efficient way to detect a very distant massive cluster and provides a unique opportunity to study mass distributions in very distant clusters. Therefore, searches for massive condensations in the field of dark lens objects by the detection of the lensing signatures with deep optical imaging and by X-ray detection is a possible direction for observational cosmology in the near future.

§5. Clusters of galaxies as natural gravitational telescopes

5.1. Looking at distant galaxies through cluster-lenses

Cluster lenses magnify and distort galaxies behind them. For an efficient cluster (a massive cluster with intermediate redshift $z \sim 0.2$ – 0.4) the magnification factor for the faint galaxy population is typically ~ 2 in a few square arc-minutes. This gain would correspond to a factor of ~ 1.5 in the diameter of a telescope or an increase by a factor of ~ 4 in exposure time. Clearly, looking through cluster lenses can be of some reward when studying a faint (and thus distant) galaxy population, as it allows us to observe intrinsically fainter objects that would not otherwise be observable when looking at blank fields. Cluster lenses do magnify but also distort the shape of distant galaxies, and the farther the source, the stronger the distortion. Hence the shape of a lensed galaxy (and whether it is multiple or not) is generally a good distance indicator. These properties have effectively been used in detail in recent years to study the faint and distant galaxy population. Thus cluster lenses have been nicknamed “natural telescope”.

Cluster lenses can be used as telescopes in two different ways, i) as magnifying glasses for non-resolved sources. Here, only the magnification property is used, to constrain galaxy counts to fainter limits, and to study photometric properties of fainter galaxies. ii) Cluster lenses can also be used as real telescopes for resolved sources. Here, both magnification and distortion properties are used to 1) constrain galaxy morphology to fainter limits, and 2) constrain their distance through their observed shape.

The high quality imaging obtained with the *HST*/WFPC2 camera provides the

key observations that make possible the use of cluster lenses as natural telescopes. Indeed, thanks to its high-resolution imaging capabilities it allows us to better identify morphologically multiple images and to accurately compute the shapes of arclets. These critical parameters are the necessary ingredients for the construction of a robust mass distribution model of cluster lenses. Furthermore, if at least one multiple image has a spectroscopic redshift, then the mass distribution model is absolutely calibrated, making a cluster lens an effective cosmological telescope.

5.2. Resolved lensed galaxies — Morphological and physical properties

Morphological properties of distant lensed sources were first addressed by Smail et al.,¹⁰⁵⁾ who estimated the intrinsic linear sizes of the galaxies and showed them to be compatible with a significant size evolution with redshift. Smail et al.¹⁰⁵⁾ studied the *HST* images of four distant massive clusters and found that the half light radius of the arcs along the radial direction of the cluster potential is a factor of 1.5–2 times smaller than the equivalent population in the local field. If the gross properties of the central regions of the cluster surface mass density at the position of the tangential arcs can be characterized by $\Sigma \sim \theta^{-1}$, the radial stretching rate is unity (see §2.1), and the above mentioned results can be taken as the intrinsic nature of the arcs. Since they showed that the $\Sigma \sim \theta^{-1}$ is a good representative of the central mass distribution of their sample clusters, they suggested that the dominant population of star-forming galaxies at $z \sim 1$ is a factor

of 1.5–2 times smaller in size than the equivalent population in the local field. If the cluster surface mass density profile obtained at the radial arc position can be extrapolated to the tangential arc position, the surface mass density is shallower than $\Sigma \propto \theta^{-1}$, and the radial width of the tangential arc is larger than the intrinsic source size. This strengthens the conclusion reached by Smail et al.¹⁰⁵⁾ Recently, a number of high- z arcs and arclets have been confirmed spectroscopically.^{14), 106) - 108)} A detailed analysis of their intrinsic size and morphology is then possible using lens modelling. More recently, several detailed analyses of the morphology of high- z arcs were reported using lens modelling. For example, Soucail et al.¹¹²⁾ found a ring galaxy LRG J0239-0134 at $z = 1$ through the cluster lens A370 (Fig. 15). The morphological nature of this object is more complex than that of nearby normal

Fig. 15. The image of the distant ring galaxy, LRG J0239-0134 at $z = 1.062 \pm 0.001$ magnified by cluster lens A370.⁴⁹⁾ *ISO/LW3* contours overplotted on *HST/WFPC2* F675W image (with a 12'' size). This object is appeared closed to the galaxy #32 but this galaxy has been subtracted for clarity (a black dot position at the right of the ring galaxy).

galaxies and is very similar to the Cartwheel galaxy,¹¹³⁾ which is thought to be an interacting galaxy. Most of them appear to be knotty with a more complex morphology than their local counterparts,^{109) - 111)} although there may be some biases due to observations in the UV rest frame.

5.3. Resolved lensed galaxies — Distances of faint populations

The probability distribution of the redshift of an arclet for a given mass distribution of the cluster and the shape of the arclet depends only on the intrinsic ellipticity distribution of faint galaxies:³²⁾ the larger the redshift, the larger (in general) the deformation induced by the cluster. From a secure mass distribution defined by a few sets of multiple-images, we can then estimate a likely value of z of arclets behind well-constrained clusters. This is most interesting, as this method is purely geometrical and therefore does not suffer from the spectroscopic bias that provides redshifts only for these faint galaxies with (strong) optical emission lines. To evaluate the accuracy of this technique on a cluster-lens **A2218**,³²⁾ Ebbels et al.¹¹⁴⁾ have successfully measured with the 4.2m *WHT* the redshift of 19 arclets, providing a first confirmation of the lensing method. Their results shows that the mean redshift of the faint field population at $R \sim 25.5$ ($B \sim 26-27$) is low, $\langle z \rangle = 0.8-1$. Similar work is now in progress for other cluster lenses, such as **A2390**¹¹⁵⁾ and **AC114**.

5.4. Non-resolved lensed galaxies in the Submm and MIR bands

A fruitful avenue that has developed in the last two years is the study of distant galaxies in until recently unexplored windows of the electromagnetic spectrum: the Mid-IR, the Sub-millimetre and Millimetre bands. Indeed, the ISOCAM camera on the *ISO* satellite and the SCUBA instrument on *JCMT*, thanks to their larger survey efficiency (compared to previous instruments), allow for studies of distant galaxies. Boosting their detecting efficiency with lensing magnification has shed new light in the nature of faint galaxies detected in these two wavebands (Fig. 16).

Distant, $z > 3$, objects were supposed to be strong sub-mm sources because we do expect to detect redshifted dust-emission from these distant galaxies.¹²²⁾ A first tentative application in sub-mm has been recently presented by Smail, Ivison and Blain.¹²¹⁾ It is now extended to cover seven clusters.¹²³⁾ They found in total 16 3σ sources and 10 4σ sources at $850\mu\text{m}$ through all seven clusters. Their sub-mm galaxy counts greatly exceed those expected in a non-evolving model based on the local *IRAS* $60\mu\text{m}$ luminosity function¹²⁴⁾ or in a model that can explain the optically selected Lyman-dropout¹²⁵⁾ and Lyman-emission samples¹²⁶⁾(Fig. 16). Smail et al.¹²⁷⁾ have attempted to find optical counterparts of these sub-mm sources using *HST* images. Counterparts were identified for 14 of the 16 3σ sources. One of them is thought to be the distant ring galaxy LRG J0239-0134 shown in Fig. 15. The morphologies of the optical counterparts fall into disturbed/interacting objects and compact objects. The disturbed and interacting galaxies constitute the largest class, which suggests that interactions play an important role in triggering star formation and nuclear activity in the distant universe.

A deep survey through cluster lenses in the mid-IR wave band ($7\mu\text{m}$ and $15\mu\text{m}$) using *ISO/ISOCAM* also has been performed.¹²⁸⁾ Currently, a total area of about

Fig. 16. Cumulative sub-mm number counts through cluster lenses and in the field.¹¹⁶⁾ The results obtained through lenses are indicated by solid squares. The results obtained by earlier works from Barger et al. (B98),¹¹⁷⁾ Eales et al. (E98),¹¹⁸⁾ Holland et al. (H98),¹¹⁹⁾ Hughes et al. (Hu98),¹²⁰⁾ and Smail et al. (SIB)¹²¹⁾ are shown by solid circles. The number counts through cluster lenses reaches down to a very faint flux density limit of 0.5mJy at 850 μ m, several times fainter than the confusion limit of the *JCMT* in blank fields.¹²⁰⁾

53 arcmin² has been covered in maps of three clusters. The source counts, corrected for cluster contamination and lensing distortion effects, exhibit an excess by a factor of 10 with respect to the prediction of a non-evolution model.¹²⁹⁾ The results suggest that abundant star formation occurs in very dusty environments at $z \sim 1$. As shown in Fig. 15, the distant ring galaxy LRG J0239-0134 is a bright mid-IR source.¹¹²⁾ The fact that the [OII] line is more extended than the underlying stellar continuum indicates on going star formation in the ring. The detection of the [NeV] emission line indicates the existence of an active nucleus. These results indicate that a galaxy-galaxy interaction triggered the formation of the star-forming ring and

nuclear activity in LRG J0239-0134.

These results indicate that interactions play an important role in triggering star formation and nuclear activity in the distant universe, and that care must be taken to take account of the dust in inferring global star formation history from UV and optical luminosities of high- z galaxies.

§6. Arc statistics

As in the case of the statistical study of the multiply imaged QSOs,¹³⁰⁾ it is natural to expect that the statistical study of arcs could be a powerful tool to study¹³¹⁾⁻¹³⁴⁾ i) the cosmological world models (and particularly to the cosmological density parameter Ω_0 and the cosmological constant Λ_0), ii) the average cluster mass distribution/profile, and iii) the nature and evolution of high redshift galaxies. Aiming to extract fruitful information regarding these topics, statistical studies of arcs have been performed by many authors. These studies have been referred to as “arc statistics”. Clearly, arc statistics depend on a large number of parameters which still contain large uncertainties, and we therefore here attempt to clarify its possible application in order to sharpen the focus for its future use.

Wu and Hammer¹³⁵⁾ provided the definition for a giant luminous arc (GLA) and performed the first quantitative comparison between the theoretically predicted number of GLAs and the observed number of GLAs. Because no observational results on systematic arc surveys had been reported, the frequency of finding GLAs in clusters was extrapolated from the reported number of GLAs at that time. They found that the frequency of finding GLAs in clusters is very sensitive to the degree of the central mass concentration in the clusters. They concluded that the observed high frequency of finding GLAs indicates a high central mass concentration in the clusters. The first well-defined GLA survey was conducted by Le Fèvre et al.¹⁵⁾ They found 6 GLAs among 15 X-ray luminous clusters. (Although their original sample contained 16 clusters, one of their samples turned out not to be a cluster.¹³⁷⁾) They selected X-ray luminous clusters with $z > 0.2$ from the EMSS. The first quantitative comparison with these survey results was performed by Hattori, Watanabe and Yamashita.¹³⁶⁾ They found that the theoretically expected number of GLAs within the framework of the circularly symmetric cluster potentials, which is consistent with X-ray observations, is two orders of magnitude less than the observed number. Molikawa et al.¹³⁷⁾ found that the radial profile of Le Fèvre et al. sample clusters have a large variation from cluster to cluster, and they are far from the radial profile adopted by Hattori, Watanabe and Yamashita.¹³⁶⁾ However, Molikawa et al.¹³⁷⁾ reached the same conclusion as Hattori, Watanabe and Yamashita.¹³⁶⁾ Hamana and Futamase¹³⁸⁾ examined the GLA statistics by taking into account the evolution of the luminosity function found by the Canada-France Redshift Survey.¹³⁹⁾ They showed that the observed evolution in the galaxy luminosity function causes the GLA number to increase by at most a factor of 2–3. These results suggest that more realistic modelling of the lens cluster potential, taking into account irregularities due to substructures and bright member galaxies, is important to account for the discrepancy. The importance of the irregularities is also claimed in the series of works

by Bartelmann and his collaborators^{140) - 143)} using numerical simulations. They¹⁴¹⁾ found that the irregular distribution of dark matter in clusters can increase the cross section of forming giant arcs by two orders of magnitude compared with the spherical symmetric mass distribution model.

As for the next step of the arc statistics, if one considers the explosive progress in the refinement of the determination of the mass distribution in individual clusters by strong and/or weak lensing observations, constraining the mass distribution of clusters using GLA statistics may not be an efficient way. The arc statistics should be studied with the well-constrained mass distribution model of the individual cluster by the detailed lensing studies best with *HST*/WFPC2 data, with the help of X-ray data. This process must be done for at least the 15 clusters in Le Fèvre et al. sample, because this sample is an unbiased sample and the best for a statistical treatment. Then the questions to be addressed using the arc statistics are those concerning the evolutionary nature of the high redshift galaxies and maybe these involved in constraining the cosmological world model. This kind of work has already been initiated by Bèzécourt.¹⁴⁴⁾ Bèzécourt studied the statistics of an arclet in A370 because the cluster mass distribution of A370 is well-constrained by lensing. It was shown that using a realistic cluster potential is essentially important to recover the observed number of arclets.

Several meaningful results for probing the high redshift universe using arc statistics have been reported. Miralda-Escudé¹³³⁾ showed that the number of GLAs responds sensitively to the intrinsic size of galaxies, and it decreases drastically when the intrinsic size of galaxies becomes smaller than the seeing FWHM. Hattori, Watanabe and Yamashita¹³⁶⁾ showed that the apparent-unlensed source size distribution of GLAs has a sharp peak at the seeing FWHM. The seeing FWHM of the current arc survey of 0."8¹⁵⁾ is about the size of the L_* spiral galaxies at $z \sim 1$ if there is no evolution in the source size, and the drop of the number in the larger source size is due to the exponential decrease of the galaxy luminosity function over L_* . Therefore, it is expected that the source galaxies of GLAs are mostly the spiral galaxies with $z < 1$. Wu and Hammer¹³⁵⁾ and Hattori, Watanabe and Yamashita¹³⁶⁾ confirmed this. Hattori, Watanabe and Yamashita¹³⁶⁾ pointed out that the fraction of GLAs which are spheroidal galaxies nearly in their forming epoch in the observed GLAs is relatively large if the SED of the UV bright elliptical is a good representative of the majority of elliptical galaxies. It is worth noting that a fraction of the GLAs and multiply imaged galaxies are made from the high redshift galaxies with $z > 2$.^{145), 146), 111)} This may suggest either a lacking in our current understanding of the evolutionary features of the high redshift galaxies or that high redshift elliptical galaxies in the formation process started to be detected as GLAs. Quantification of the star formation rate in the GLAs by multi-band observations, especially in MIR and sub-mm wave bands mentioned in §5, may answer to this question soon.

A more extended arc survey for an unbiased sample containing a much larger number of clusters is of course important.¹⁴⁷⁾ The cluster sample provided by the *ROSAT* all-sky survey is undoubtedly a good unbiased sample for the arc survey. It is also expected that a new, better cluster sample will be provided by an all-sky survey in the 2–10keV band, which is more appropriate for detecting clusters than

the *ROSAT* band, planned to be performed by the X-ray satellite *ABRIXAS*¹⁴⁸⁾ soon.

Topics in connection with cosmological constraints are presented in the next section.

§7. Cosmological constraint by cluster lensing

7.1. Constraints from arc statistics

Bartelmann et al.¹⁴³⁾ performed a set of cosmological N -body simulations, and found that the optical depths for the formation of giant arcs is sensible for the cosmological world models and is the largest for the low Ω_0 cold dark matter model (OCDM). They concluded that the OCDM is likely to be the only model which can match current observations of the giant arc survey. These differences originate from the different epochs of cluster formation among the cosmological models. They found that clusters with $z \sim 0.2$ – 0.6 , which are the most responsible for the formation of arcs, in the OCDM exhibit the most irregular shape in mass distribution, and as a result they have the strongest shear, since the cluster formation epoch is just around this redshift range in this model. This is very interesting and a practical variation of the idea that uses the degree of inhomogeneity in cluster mass distributions to constrain Ω_0 first proposed by Richstone, Loeb and Turner.¹⁴⁹⁾ One of the weakness of this kind of method is that the observable, that is the degree of inhomogeneity, to be compared with the model prediction is somewhat abstract. However, Bartelmann et al.¹⁴³⁾ made quantitative comparison possible by connecting with arc statistics. However, the contribution of the bright member galaxies are not taken into account because of their numerical resolution limit, although they clearly have central role in cluster strong lensing, as shown in §3. Further improvement of numerical simulations is required.

The redshift distribution of the GLAs have been proposed to constrain the cosmological constant.¹⁵⁰⁾ However, the redshift distribution of the GLAs is very sensitive to the mass distribution model of the cluster. It requires a very accurate modelling of the cluster mass distribution to constrain the cosmological constant. Further, the expected number of GLAs in one cluster is less than 1. We must perform an arc survey for a large number of clusters for which the mass distribution is precisely constrained. This will be a difficult task, but it is required to be done.

7.2. Cosmological constraints using (Ω_0, A_0) dependence of D_{ds}/D_s and $\omega(z)$

The combination of the angular diameter distance appears in the lens equation as D_{ds}/D_s , and its value depends only on the cosmological constant.¹⁵¹⁾ Using this fact, several methods to constrain the cosmological constant have been proposed. The merit of this kind of method is that one cluster is enough to provide a stringent constraint on the cosmological constant. However, the demerit is that the mass distribution of the cluster must be measured very precisely. One variation of this

method is using the lensing factor $\omega(z)$ defined as

$$\omega(z) \equiv \frac{D_{\text{ds}}(z)/D_{\text{s}}(z)}{D_{\text{ds}}(\infty)/D_{\text{s}}(\infty)}. \quad (7.1)$$

The convexity of the lensing factor has a (Ω_0, Λ_0) dependence. Gautret, Fort and Mellier¹⁶¹⁾ proposed the triplet method, in which (Ω_0, Λ_0) is constrained by using this dependence. The advantage of the triplet method is that it does not require the accurate measurement of the cluster mass distribution. Although the Freedman distance is used as the angular diameter distance in these methods, it is likely that there is a variation of the angular diameter distance from line-of-sight to line-of-sight due to the inhomogeneity of the universe.^{152), 153)} Therefore, the quantitative calibration of the variation of the angular diameter distance is an important complementary works to extract reliable results from these methods. In this section, three methods proposed to constrain (Ω_0, Λ_0) following the above mentioned principle are summarized.

7.2.1. Constraints from depletion curve

Broadhurst¹⁵⁴⁾ first found that the galaxy number count in the direction of the cluster exhibits diagnostics which are now called the “depletion curve”. Since the detail nature of the depletion curve depends on the magnification due to the cluster lens, he proposed to use it for measuring the cluster mass. Fort, Mellier and Dantel-Fort¹⁵⁵⁾ pointed out that the depletion curve can be used to constrain the cosmological constant if the mass distribution of the cluster is accurately measured. The expected galaxy number density in the direction of the lensing cluster is

$$N(r) = N_0 \mu(r)^{2.5\alpha-1}, \quad (7.2)$$

where μ is the magnification at the position r and $\alpha = d \log(N)/dm$ is the slope of the galaxy number counts. The first term of the exponent, 2.5α , describes the increase of the galaxy number density, since fainter galaxies become brighter than the limiting magnitude due to the lensing magnification. The last term of the exponent, -1 , describes the decrease of the galaxy number density, since the unit solid angle area of the unlensed source plane becomes a factor of μ larger due to lensing, and the galaxy number within the unit solid angle of the lensed source plane decreases a factor of $1/\mu$. Since the slope of the galaxy number counts is $\sim 0.17 \pm 0.02$,^{155) - 157)} less than 0.4, the galaxy number density through a cluster decreases. Therefore the radial profile of the galaxy number counts through a cluster is called the “depletion curve”. The main idea to constrain the cosmological constant by using the depletion curve, is as follows. At the Einstein ring radius the magnification is infinite and the depletion curve reaches zero as its minimum value. The Einstein ring radius becomes larger for a higher redshift source and converges into a finite radius for sources at the infinite redshift. The Einstein ring radius for sources with infinite redshift is referred to the “last critical line”. The observed depletion curve is the superposition of these depletion curves of different source redshifts. The last critical line can be identified as the dip in the depletion curve appearing at the largest radius. Since the radius of the last critical line is larger for larger cosmological constants for a

fixed cluster mass distribution model, the cosmological constant can be constrained by identifying the last critical line for the cluster for which the mass distribution is well constrained. Fort, Mellier and Dantel-Fort¹⁵⁵⁾ applied it to CL0024+17 and constrained the cosmological constant to be larger than 0.6. The merit of this method is that the cosmological constant can be constrained with only one well-studied cluster. However, the cluster mass distribution model used by them is likely to be far from reality since there is evidence of the superposition of two large clusters in the line-of-sight,⁴⁹⁾ and the detection of the last critical line for this cluster is also not so clear. A revised lens modelling and observational studies with deeper imaging are necessary to extract a clear conclusion on the value of the cosmological constant.

7.2.2. GRAMORs

Futamase, Hattori and Hamana¹⁵⁸⁾ predicted the existence of a highly magnified gravitationally lensed yet morphologically regular images (they referred to as GRAMORs) in clusters of galaxies and proposed a new method to constrain the cosmological constant by using the GRAMORs.^{159), 146)} A marginally critical lens cluster may have GRAMORs if the source galaxy is located close to the line of sight through the cluster center. The lowest source redshift for which the cluster can have GRAMORs is lower for a larger cosmological constant for a fixed cluster mass distribution model. Clusters with intermediate X-ray luminosities are favored to give a lower limit on the cosmological constant, since the difference of the possible lowest source redshift of the GRAMORs with and without the cosmological constant is largest for those clusters. If one identifies a very low redshift GRAMOR, it is sufficient to give a stringent lower limit on the cosmological constant. The merit compared with the depletion curve method, where we have to rely on the photometric method to measure the source redshift, is that the redshift of the GRAMORs is spectroscopically measurable.

Although these two methods require only one cluster to constrain the cosmological constant in principle, a precise measurement of the cluster mass distribution is required. It is practically very hard.

7.2.3. The triplet method

Attempts to disentangle the coupling between the cosmological parameters, the source redshift and the lens modelling have been made by Lombardi and Bertin¹⁶⁰⁾ and Gautret, Fort and Mellier.¹⁶¹⁾ In particular, the triplet method proposed by Gautret, Fort and Mellier¹⁶¹⁾ does not require to know the detail of the cluster mass distribution and is summarized in this section. The ellipticity parameter, ϵ , for a circular source at z_i is obtained by

$$\epsilon = \frac{\omega_i \gamma_\infty}{1 - \omega_i \kappa_\infty}, \quad (7.3)$$

where the subscripts i refers to the redshift z_i , γ_∞ and κ_∞ are the shear and the convergency for the source at infinite redshift, and the ellipticity is defined as

$$\epsilon = \frac{1 - r}{1 + r}. \quad (7.4)$$

Here r is the axis ratio of the image isophotes. Take three galaxies with different redshifts at z_i , z_j and z_k , which are located close together in the sky through the lensing cluster and name these “triplet”. Because of the proximity of the triplet in the sky, the local convergence κ_∞ and shear γ_∞ can be assumed equal all three. The triplet of galaxies gives three sets of Eq. (7.3). The quantities κ_∞ and γ_∞ can be deleted from these equations, and a final equation independent of both on κ_∞ and γ_∞ can be derived, such as

$$\begin{vmatrix} 1 & \omega_i & \omega_i g_j g_k \\ 1 & \omega_j & \omega_j g_k g_i \\ 1 & \omega_k & \omega_k g_i g_j \end{vmatrix} = 0. \quad (7.5)$$

The final equation is satisfied only when we assume correct values of the real universe for (Ω_0, Λ_0) . Then the problem is reduced to determining for the (Ω_0, Λ_0) values which satisfy the final equation. Unfortunately, the method is degenerate in (Ω_0, Λ_0) . Therefore, a complementary cosmological constraint, such as a high-redshift supernovae,¹⁶²⁾ is required to break the degeneracy. It is also pointed out that the triplet method is able to measure directly the curvature of the universe, $1 - \Omega_0 - \Lambda_0$, because of the mean orientation of its degeneracy. Although in the above discussion the source intrinsic ellipticity was omitted, errors introduced by the intrinsic ellipticity must be taken into account. Since the orientation and the ellipticity of the source intrinsic shape are likely to be random, it will be canceled out if we average over many sources. Errors in the source redshift due to the limitation of the photometric redshift method and systematics due to the possible multiple lens plane, e.g., the lensing of the galaxies at z_j and z_k by a galaxy at z_i , where z_i is the lowest within the triplet, also introduces errors in the obtained cosmological parameters. Therefore, applying the triplet method to many clusters is desired. Gautret, Fort and Mellier¹⁶¹⁾ have undertaken an intensive study on possible error estimates and have concluded that the observation of 100 clusters can separate the $\Omega_0 = 0.3$ and $\Omega_0 = 1$ universe with a 2σ confidence level and could be a good subject for VLT and NGST.

§8. Conclusion

We have seen how fruitful the cluster lensing studies are. Surprisingly, almost all areas described in this review are realizations of Zwicky’s dream. It is no doubt that cluster lensing will play central role as one of the standard techniques to study the evolutionary history of the mass distribution of the universe, to probe the deep universe, and to constrain the cosmological world models in the next decade with the combination of revolutionary new observational instruments from radio to X-ray, which already have emerged and will emerge during the next decade.

Acknowledgements

The authors are very grateful to K. Tomita and T. Futamase for providing an opportunity to write this review at the right time and for their patience. MH wishes to

thank K. Hashimoto-dani for allowing pre-publication of some of his original figures, and thanks M. Murata for providing useful programs to draw caustics and time-delay surfaces. JPK thanks financial supports of CNRS-INSU and Yamada Science Foundation for fruitful visit to Japan. MH thanks financial supports of Yamada Science Foundation, and Grants-in-Aid by the Ministry of Education, Science and Culture of Japan (09740169, 60010500) in the course of the most of our studies summarized in this review.

References

- 1) R. Lynds and V. Petrosian, *Bulletin of the American Astronomical Society* **18** (1986), 1014.
- 2) G. Soucail, B. Fort, Y. Mellier and J. P. Picat, *Astron. Astrophys. Lett.* **172** (1987), L14.
- 3) G. Soucail, Y. Mellier, B. Fort and M. Cailloux, *Astron. Astrophys. Lett.* **191** (1988), L19.
- 4) B. Paczyński, *Nature* **325** (1987), 572.
- 5) F. Zwicky, *Phys. Rev.* **51** (1937), 290.
- 6) F. Zwicky, *Phys. Rev.* **51** (1937), 679.
- 7) K. Umetsu, M. Tada and T. Futamase, *Prog. Theor. Phys. Suppl. No. 133* (1999), 53.
- 8) R. D. Blandford and C. S. Kochaneck, “Gravitational lenses” in *Dark matter in the universe*, ed. J. Bahcall, T. Piran and S. Weinberg, (World Scientific, Singapore, 1987).
- 9) R. D. Blandford and R. Narayan, *Annu. Rev. Astron. Astrophys.* **30** (1992), 311.
- 10) P. Schneider, J. Ehlers and E. E. Falco, *Gravitational Lenses* (Springer-Verlag, Berlin, 1992).
- 11) B. Fort and Y. Mellier, *Astron. Astrophys. Rev.* **5** (1994), 239.
- 12) X.-P. Wu, *Fund. Cosm. Phys.* **17** (1996), 1.
- 13) R. Narayan and M. Bartelmann, Preprint astro-ph/9606001.
- 14) Y. Mellier, *Annu. Rev. Astron. Astrophys.* **37** (1999), in press.
- 15) O. Le Fèvre, F. Hammer, M. C. Angonin, I. M. Gioia and G. A. Luppino, *Astrophys. J. Lett.* **422** (1994), L5.
- 16) E. L. Turner, J. P. Ostriker and J. R. Gott III, *Astrophys. J.* **284** (1984), 1.
- 17) J. F. Navarro, C. S. Frenk and S. D. M. White, *Astrophys. J.* **490** (1997), 493.
- 18) M. Bartelmann, *Astron. Astrophys.* **313** (1996), 697.
- 19) D. Maoz, H.-W. Rix, A. Gal-Yam and A. Gould, *Astrophys. J.* **486** (1997), 75.
- 20) Y. Mellier, B. Fort and J.-P. Kneib, *Astrophys. J.* **407** (1993), 33.
- 21) I. Kovner, *Astrophys. J.* **337** (1989), 621.
- 22) D. Merritt and L. Hernquist, *Astrophys. J.* **376** (1991), 439.
- 23) R. R. Bourassa, R. Kantowski and T. D. Norton, *Astrophys. J.* **185** (1973), 747.
- 24) K. Asano and T. Fukuyama, *Publ. Astron. Soc. Jpn.* **100** (1998), 100.
- 25) A. Kassiola and I. Kovner, *Astrophys. J.* **450** (1993), 450.
- 26) R. D. Blandford and R. Narayan, *Astrophys. J.* **310** (1986), 568.
- 27) T. Poston and I. Steward, *Catastrophe theory and its applications* (Pitman, London, 1978).
- 28) R. Pelló, J.-F. Le Borgne, G. Soucail, Y. Mellier and B. Sanahuja, *Astrophys. J.* **366** (1991), 405.
- 29) G. Mathez, G. Fort, Y. Mellier, J.-P. Picat and G. Soucail, *Astron. Astrophys.* **256** (1992), 343.
- 30) J.-P. Kneib, Y. Mellier, B. Fort and G. Mathez, *Astron. Astrophys.* **273** (1993), 367.
- 31) J. Bézecourt, J.-P. Kneib, G. Soucail and T. M. D. Ebbels, Preprint astro-ph/9810199.
- 32) J.-P. Kneib, R. S. Ellis, I. Smail, W. J. Couch and R. M. Sharples, *Astrophys. J.* **471** (1996), 643.
- 33) P. Natarajan, J.-P. Kneib, I. Smail and R. S. Ellis, *Astrophys. J.* **499** (1998), 600.
- 34) B. Geiger and P. Schneider, *Mon. Not. R. Astron. Soc.* **302** (1998), 118.
- 35) J. E. Trümper, *Physica Scripta* **T7** (1994), 209.
- 36) J. A. Tyson, G. P. Kochanski and I. P. Dell’Antonio, *Astrophys. J. Lett.* **498** (1998), L107.
- 37) Y. Tanaka, H. Inoue and S. S. Holt, *Publ. Astron. Soc. Jpn.* **46** (1994), L37.
- 38) P. J. E. Peebles, *Principles of Physical Cosmology* (Princeton University Press, Princeton, 1993).

- 39) A. Loeb and S. Mao, *Astrophys. J. Lett.* **435** (1994), L109.
- 40) J. Miralda-Escudè and A. Babul, *Astrophys. J.* **449** (1995), 18.
- 41) X.-P. Wu and L. Z. Fang, *Astrophys. J.* **483** (1997), 62.
- 42) N. Ota, K. Mitsuda and Y. Fukazawa, *Astrophys. J.* **495** (1998), 170.
- 43) X.-P. Wu, T. Chiueh, L.-Z. Fang and Y.-J. Xue, *Mon. Not. R. Astron. Soc.* **301** (1998), 861.
- 44) K. Hashimoto-dani, PhD dissertation, Oosaka Univ. (1999) in preparation.
- 45) S. W. Allen, *Mon. Not. R. Astron. Soc.* **296** (1998), 392.
- 46) N. Makino, *Astrophys. J.* **490** (1997), 642.
- 47) K.-T. Kim, P. P. Kronberg, G. Giovannini and T. Venturi, *Nature* **341** (1989), 720.
- 48) C. I. Sarazin, *Rev. Mod. Phys.* **58** (1986), 1.
- 49) G. Soucail, N. Ota, H. Böhringer, O. Czoske and M. Hattori, (1999) in preparation.
- 50) O. Czoske, J.-P. Kneib, G. Soucail, Y. Mellier and T. Bridges, (1999) in preparation.
- 51) W. Forman, "Clusters of galaxies and cooling hot gas" in *Cooling Flows in Clusters and Galaxies*, ed. A. C. Fabian (Kluwer Academic Publishers, London, 1988), p.17.
- 52) A. C. Fabian, *Annu. Rev. Astron. Astrophys.* **32** (1994), 277.
- 53) S. W. Allen, A. C. Fabian and J.-P. Kneib, *Mon. Not. R. Astron. Soc.* **279** (1996), 615.
- 54) Y. Ikebe, PhD dissertation, The University of Tokyo (1996).
- 55) E. Komatsu, T. Kitayama, Y. Suto, M. Hattori, R. Kawabe, H. Matsuo, S. Schindler and K. Yoshikawa, *Astrophys. J. Lett.* **516** (1999), L1.
- 56) M. Hattori, E. Komatsu, et al., (1999), in preparation.
- 57) A. C. Edge, R. J. Ivison, I. Smail, A. W. Blain and J.-P. Kneib, *Mon. Not. R. Astron. Soc.* (1999), in press.
- 58) J.-P. Kneib, Y. Mellier, R. Pelló, J. Miralda-Escudé, J.-F. Le Borgne, H. Böhringer and J.-P. Picat, *Astron. Astrophys.* **303** (1995), 27.
- 59) R. F. Mushotzky and C. A. Scharf, *Astrophys. J. Lett.* **482** (1997), L13.
- 60) M. Birkinshaw and J. P. Hughes, *Astrophys. J.* **420** (1994), 33.
- 61) N. Makino and K. Asano, *Astrophys. J.* (1999), in press.
- 62) M. Pierre, J. F. Le Borgne, G. Soucail and J.-P. Kneib, *Astron. Astrophys.* **311** (1996), 413.
- 63) H. Böhringer, Y. Tanaka, R. F. Mushotzky, Y. Ikebe and M. Hattori, *Astron. Astrophys.* **334** (1998), 789.
- 64) M. Hattori, H. Matsuzawa, K. Morikawa, J.-P. Kneib, K. Yamashita, K. Watanabe, H. Böhringer and T. G. Tsuru, *Astrophys. J.* **503** (1998), 593.
- 65) J.-P. Kneib, J. Melnick and Gopal-Krishna, *Astron. Astrophys. Lett.* **290** (1994), L25.
- 66) J. Melnick, B. Altieri, Gopal-Krishna and E. Giraud, *Astron. Astrophys. Lett.* **271** (1993), L5.
- 67) K. Hashimoto-dani, M. Hattori, H. Katayama, M. Murata, H. Böhringer, Y. Ikebe, K. Hayashida and E. Miyata, (1999b), in preparation.
- 68) S. L. Moris, J. B. Hutchings, R. G. Carlberg, H. K. C. Yee, E. Elligson, M. L. Balogh, R. G. Abraham and T. A. Smecker-Hane, *Astrophys. J.* **507** (1998), 84.
- 69) E. Elligson, H. K. C. Yee, R. G. Abraham, S. L. Moris, R. G. Carlberg and T. A. Smecker-Hane, *Astrophys. J. Suppl.* **113** (1997), 1.
- 70) S. Schindler, L. Guzzo, H. Ebeling, H. Böhringer, G. Chincarini, C. A. Collins, S. De Grandi, D. M. Neumann, U. G. Briel, P. Shaver and G. Vettolani, *Astron. Astrophys. Lett.* **299** (1995), L9.
- 71) P. Fisher and A. J. Tyson, *Astron. J.* **114** (1997), 14.
- 72) S. Schindler, M. Hattori, D. M. Neumann and H. Böhringer, *Astron. Astrophys.* **317** (1997), 646.
- 73) B. Fort, O. Le Fèvre, F. Hammer and M. Cailloux, *Astrophys. J. Lett.* **399** (1992), L125.
- 74) I. M. Gioia, E. J. Shaya, O. Le Fèvre, E. E. Falco, G. A. Luppino and F. Hammer, *Astrophys. J.* **497** (1998), 573.
- 75) J.-P. Kneib et al., (1999), private communication.
- 76) F. Hammer, I. M. Gioia, E. J. Shaya, P. Teyssandier, O. Le Fèvre and G. A. Luppino, *Astrophys. J.* **491** (1997), 477.
- 77) T. Fukushige and J. Makino, *Astrophys. J. Lett.* **477** (1997), L9.
- 78) Y. Fujita and F. Takahara, preprint (1999a).
- 79) W. H. Press and P. Schechter, *Astrophys. J.* **187** (1974), 425.

- 80) C. G. Lacey and S. Cole, *Mon. Not. R. Astron. Soc.* **262** (1993), 627.
- 81) A. W. Blain and M. S. Longair, *Mon. Not. R. Astron. Soc.* **265** (1993), L21.
- 82) S. Sasaki, *Publ. Astron. Soc. Jap.* **46** (1994), 427.
- 83) T. Kitayama and Y. Suto, *Mon. Not. R. Astron. Soc.* **280** (1996), 638.
- 84) Y. Fujita and F. Takahara, preprint (1999b).
- 85) T. Wiklind and F. Combes, *Nature* **379** (1996), 139.
- 86) M. Hattori, Preprint astro-ph/9711156.
- 87) M. Hattori, Y. Ikebe, I. Asaoka, T. Takeshima, H. Böhringer, T. Mihara, D. M. Neumann, S. Schindler, T. Tsuru and T. Tamura, *Nature* **388** (1997), 146.
- 88) C. R. Lawrence, D. P. Schneider, M. Schmit, C. L. Bennett, J. N. Hewitt, B. F. Burke, E. L. Turner and J. E. Gunn, *Science* **223** (1984), 46.
- 89) D. P. Schneider, C. R. Lawrence, M. Schmidt, J. E. Gunn, E. L. Turner, B. F. Burke and V. Dhawan, *Astrophys. J.* **294** (1985), 66.
- 90) G. Langston, J. Fisher and C. Aspin, *Astron. J.* **102** (1991), 1253.
- 91) D. Narasimha, K. Subramanian and S. M. Chitre, *Astrophys. J.* **315** (1987), 434.
- 92) J.-P. Kneib, G. Soucaïl, A. Jaunsen, M. Hattori, J. Hjorth and T. Yamada, *CFHT Information Bulletin* **38** (1998), 12.
- 93) N. Benítez, T. Broadhurst, P. Rosati, F. Courbin, G. Squires, C. Lidman and P. Magain, Preprint astro-ph/9812218.
- 94) T. Kodama, N. Arimoto, A. J. Barger and A. Aragón-Salamanca, *Astron. Astrophys.* **334** (1998), 99.
- 95) N. A. Bahcall, L. M. Lubin and V. Dorman, *Astrophys. J. Lett.* **447** (1995), L81.
- 96) D. W. Weedman, R. J. Weyman, R. F. Green and T. M. Heckman, *Astrophys. J. Lett.* **255** (1982), L5.
- 97) J. A. Tyson, P. Seitzer, R. J. Weymann and C. Foltz, *Astron. J.* **91** (1986), 1274.
- 98) P. Fischer, J. A. Tyson, G. M. Bernstein and P. Guhathakurta, *Astrophys. J. Lett.* **431** (1994), L71.
- 99) C. B. Foltz, R. J. Weymann, H.-J. Röser and F. H. Chaffee Jr., *Astrophys. J. Lett.* **281** (1984), L1.
- 100) C. C. Steidel and W. L. W. Sargent, *Astron. J.* **102** (1991), 1610.
- 101) H. Bonnet, B. Fort, J.-P. Kneib, Y. Mellier and G. Soucaïl, *Astron. Astrophys. Lett.* **280** (1993), L7.
- 102) L. van Waerbeke, Y. Mellier, P. Schneider, B. Fort and G. Mathez, *Astron. Astrophys.* **317** (1997), 303.
- 103) Y. Mellier, M. Dantel-Fort, B. Fort and H. Bonnet, *Astron. Astrophys.* **289** (1994), 15.
- 104) R. Pelló, J. M. Miralles, J.-F. Le Borgne, J.-P. Picat, G. Soucaïl and G. Bruzual, *Astron. Astrophys.* **314** (1996), 73.
- 105) I. Smail, A. Dressler, J.-P. Kneib, R. S. Ellis, W. J. Couch, R. M. Sharples and A. Oemler Jr., *Astrophys. J.* **469** (1996), 508.
- 106) T. M. D. Ebbels, J. F. Le Borgne, R. Pelló, R. S. Ellis, J.-P. Kneib, I. Smail and B. Sanahuja, *Mon. Not. R. Astron. Soc. Lett.* **281** (1996), L75.
- 107) S. C. Trager, S. M. Faber, A. Dressler and A. Oemler, *Astrophys. J.* **485** (1997), 92.
- 108) B. Frye and T. Broadhurst, *Astrophys. J. Lett.* **499** (1998), L115.
- 109) W. N. Colley, A. Tyson and E. L. Turner, *Astrophys. J. Lett.* **461** (1996), L83.
- 110) M. Franx, G. D. Illingworth, D. D. Kelson, P. G. van Dokkum and K.-V. Tran, *Astrophys. J. Lett.* **486** (1997), L75.
- 111) R. Pelló, J.-P. Kneib, J. F. Le Borgne, J. Bézecourt, T. M. Ebbels, I. Tijera, G. Bruzual, J. M. Miralles, I. Smail and T. J. Bridges, Preprint astro-ph/9810390.
- 112) G. Soucaïl, J.-P. Kneib, J. Bézecourt, L. Metcalfe, B. Altieri and J.-F. Le Borgne, Preprint astro-ph/9901123.
- 113) C. Struck, P. N. Appleton, K. D. Borne and R. A. Lucas, *Astron. J.* **112** (1996), 1868.
- 114) T. Ebbels, R. Ellis, J.-P. Kneib, J.-F. Le Borgne, R. Pelló, I. Smail and B. Sanahuja, *Mon. Not. R. Astron. Soc.* (1998), submitted.
- 115) J.-P. Kneib, R. Pelló, R. S. Ellis, I. Smail and J.-F. Le Borgne, (1999), in preparation.
- 116) A. W. Blain, J.-P. Kneib, R. J. Ivison and I. Smail, Preprint astro-ph/9812412.
- 117) A. J. Barger, L. L. Cowie, D. B. Sanders, E. Fulton, Y. Taniguchi, Y. Sato, K. Kawara and H. Okuda, *Nature* **394** (1998), 248.
- 118) S. A. Ealse, S. J. Lilly, W. K. Gear, J. R. Bond, L. Dunne, F. Hammer, O. Le Fèvre and

- D. Crampton, *Astrophys. J.* (1999), in press.
- 119) W. S. Holland, E. I. Robson, W. K. Gear, et al., *Mon. Not. R. Astron. Soc.* (1999), in press.
- 120) D. Hughes, S. Serjeant, J. Dunlop, et al. *Nature* **394** (1998), 241.
- 121) I. Smail, R. J. Ivison and A. W. Blain, *Astrophys. J. Lett.* **490** (1997), L5.
- 122) A. W. Blain, *Mon. Not. R. Astron. Soc.* **283** (1997), 1340.
- 123) I. Smail, R. J. Ivison, A. W. Blain and J.-P. Kneib, *Astrophys. J. Lett.* **507** (1998a), L21.
- 124) W. Saunders, M. Rowan-Robinson, A. Lawrence, G. Efstathiou, N. Kaiser, R. S. Ellis and C. S. Frenk, *Mon. Not. R. Astron. Soc.* **242** (1990), 318.
- 125) P. Madau, H. C. Ferguson, M. E. Dickinson, M. Giavalisco, C. S. Steidel and A. Fruchter, *Mon. Not. R. Astron. Soc.* **283** (1996), 1388.
- 126) E. M. Hu, L. L. Cowie and R. G. McMahon, Preprint astro-ph/9803011.
- 127) I. Smail, R. J. Ivison, A. W. Blain and J.-P. Kneib, Preprint astro-ph/9810281.
- 128) L. Metcalfe, B. Altieri, B. McBreen, J.-P. Kneib, M. Delaney, A. Biviano, M. F. Kessler, K. Leech, K. Okumura, B. Schulz, D. Elbaz and H. Aussel, Preprint astro-ph/9901147.
- 129) B. Altieri, L. Metcalfe, J.-P. Kneib, B. McBreen, H. Aussel, A. Biviano, M. Delaney, D. Elbaz, K. Leech, L. Lémonon, K. Okumura, R. Pelló and B. Schulz, Preprint astro-ph/9810480.
- 130) M. Chiba and T. Futamase, *Prog. Theor. Phys. Suppl. No. 133* (1999), 115.
- 131) R. J. Nemiroff and A. Dekel, *Astrophys. J.* **344** (1989), 51.
- 132) J. Miralda-Escudé, *Astrophys. J.* **403** (1993), 497.
- 133) J. Miralda-Escudé, *Astrophys. J.* **403** (1993), 509.
- 134) S. A. Grossman and P. Saha, *Astrophys. J.* **431** (1994), 74.
- 135) X.-P. Wu and F. Hammer, *Mon. Not. R. Astron. Soc.* **262** (1993), 187.
- 136) M. Hattori, K. Watanabe and K. Yamashita, *Astron. Astrophys.* **319** (1997), 764.
- 137) K. Molikawa, M. Hattori, J.-P. Kneib and K. Yamashita, *Astron. Astrophys.* (1999), accepted.
- 138) T. Hamana and T. Futamase, *Mon. Not. R. Astron. Soc.* **286** (1997), L7.
- 139) S. J. Lilly, L. Tresse, F. Hammer, M. C. Angonin, I. M. Gioia and G. A. Luppino, *Astrophys. J.* **455** (1995), 108.
- 140) M. Bartelmann and A. Weiss, *Astron. Astrophys.* **287** (1994), 1.
- 141) M. Bartelmann, M. Steinmetz and A. Weiss, *Astron. Astrophys.* **297** (1995), 1.
- 142) M. Bartelmann and M. Steinmetz, *Mon. Not. R. Astron. Soc.* **283** (1996), 431.
- 143) M. Bartelmann, A. Huss, J. M. Colberg, A. Jenkins and F. R. Pearce, *Astron. Astrophys.* **330** (1998), 1.
- 144) J. Bézecourt, Preprint astro-ph/9802107.
- 145) H. K. C. Yee, E. Ellingson, J. Bechtold, R. G. Carlberg and J.-C. Cuillandre, *Astron. J.* **111** (1996), 1783.
- 146) S. Seitz, R. P. Saglia, R. Bender, U. Hopp, P. Belloni and B. Ziegler, *Mon. Not. R. Astron. Soc.* **298** (1998), 945.
- 147) G. A. Luppino, I. M. Gioia, F. Hammer, O. Le Fèvre and J. A. Annis, Preprint astro-ph/9812355.
- 148) <http://wave.xray.mpe.mpg.de/abrixas>
- 149) D. O. Richstone, A. Loeb and E. L. Turner, *Astrophys. J.* **393** (1992), 477.
- 150) X.-P. Wu and S. Mao, *Astrophys. J.* **463** (1996), 404.
- 151) J. Miralda-Escudé, *Astrophys. J.* **370** (1991), 1.
- 152) T. Hamana, PhD dissertation, Tohoku University, (1999).
- 153) K. Tomita, H. Asada and T. Hamana, *Prog. Theor. Phys. Suppl. No.133* (1999), 155.
- 154) T. Broadhurst, Preprint astro-ph/9511150.
- 155) B. Fort, Y. Mellier and M. Dantel-Fort, *Astron. Astrophys.* **321** (1996), 353.
- 156) A. J. Tyson, *Astron. J.* **96** (1988), 1.
- 157) I. Smail, D. Hogg, L. Yan and J. G. Cohen, *Astrophys. J. Lett.* **449** (1995), L105.
- 158) T. Futamase, M. Hattori and T. Hamana, *Astrophys. J. Lett.* **508** (1998), L47.
- 159) T. Hamana, M. Hattori, H. Ebeling, J. P. Henry, T. Futamase and Y. Shioya, *Astrophys. J.* **484** (1997), 574.
- 160) M. Lombardi and G. Bertin, Preprint astro-ph/9806282.
- 161) L. Gautret, B. Fort and Y. Mellier, Preprint astro-ph/9812388.
- 162) S. Perlmutter, G. Aldering, S. Deustua et al., Preprint astro-ph/9812473.

This figure "fig2a.gif" is available in "gif" format from:

<http://arxiv.org/ps/astro-ph/9905009v1>

This figure "fig2b.gif" is available in "gif" format from:

<http://arxiv.org/ps/astro-ph/9905009v1>

This figure "fig3a.gif" is available in "gif" format from:

<http://arxiv.org/ps/astro-ph/9905009v1>

This figure "fig3b.gif" is available in "gif" format from:

<http://arxiv.org/ps/astro-ph/9905009v1>

This figure "fig3c.gif" is available in "gif" format from:

<http://arxiv.org/ps/astro-ph/9905009v1>

This figure "fig3d.gif" is available in "gif" format from:

<http://arxiv.org/ps/astro-ph/9905009v1>

This figure "fig3e.gif" is available in "gif" format from:

<http://arxiv.org/ps/astro-ph/9905009v1>

This figure "fig4a.gif" is available in "gif" format from:

<http://arxiv.org/ps/astro-ph/9905009v1>

This figure "fig4b.gif" is available in "gif" format from:

<http://arxiv.org/ps/astro-ph/9905009v1>

This figure "fig6a.gif" is available in "gif" format from:

<http://arxiv.org/ps/astro-ph/9905009v1>

This figure "fig6b.gif" is available in "gif" format from:

<http://arxiv.org/ps/astro-ph/9905009v1>

This figure "fig6c.gif" is available in "gif" format from:

<http://arxiv.org/ps/astro-ph/9905009v1>

This figure "fig7a.gif" is available in "gif" format from:

<http://arxiv.org/ps/astro-ph/9905009v1>

This figure "fig7b.gif" is available in "gif" format from:

<http://arxiv.org/ps/astro-ph/9905009v1>

This figure "fig7c.gif" is available in "gif" format from:

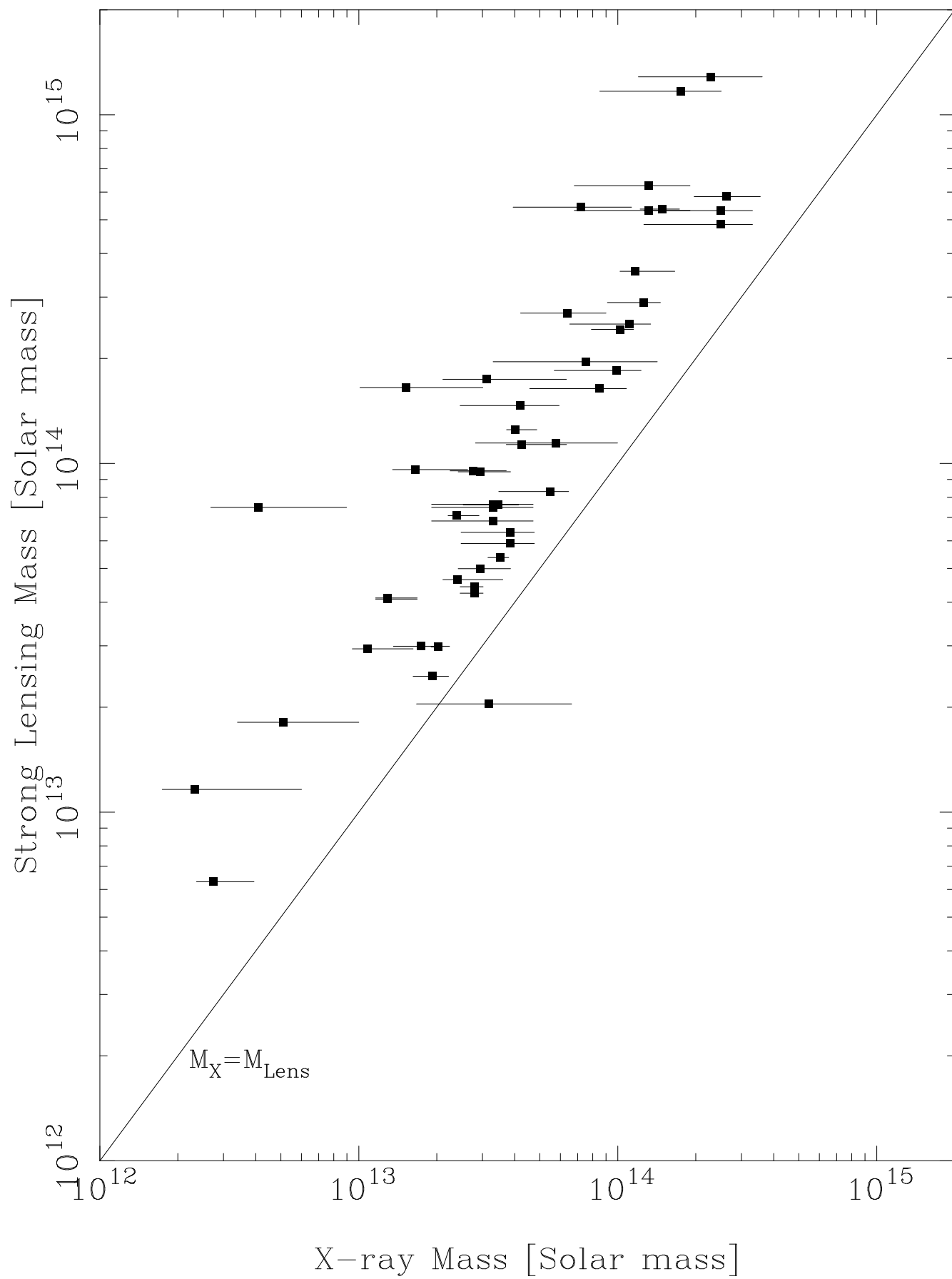
<http://arxiv.org/ps/astro-ph/9905009v1>

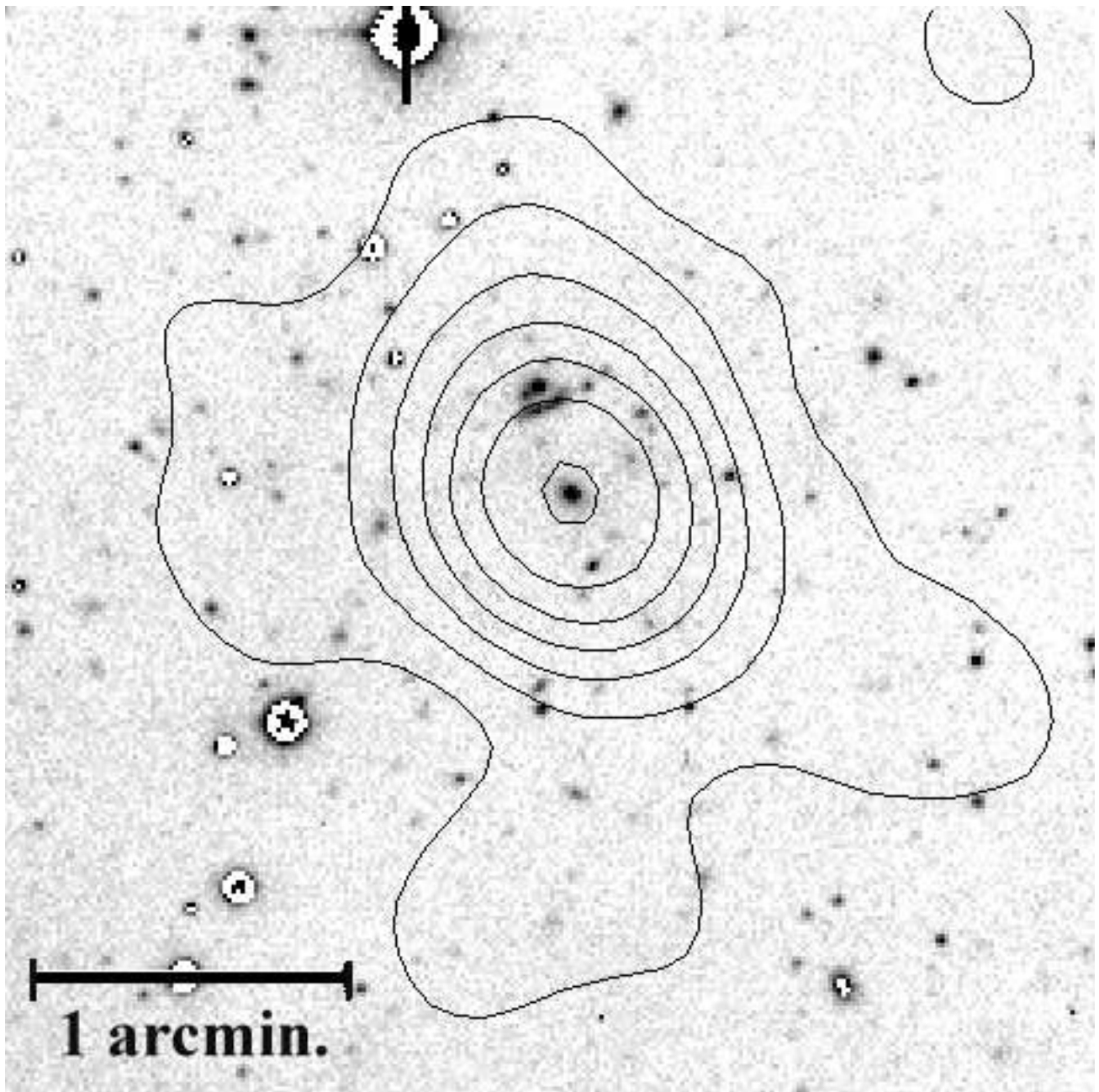
This figure "fig7f.gif" is available in "gif" format from:

<http://arxiv.org/ps/astro-ph/9905009v1>

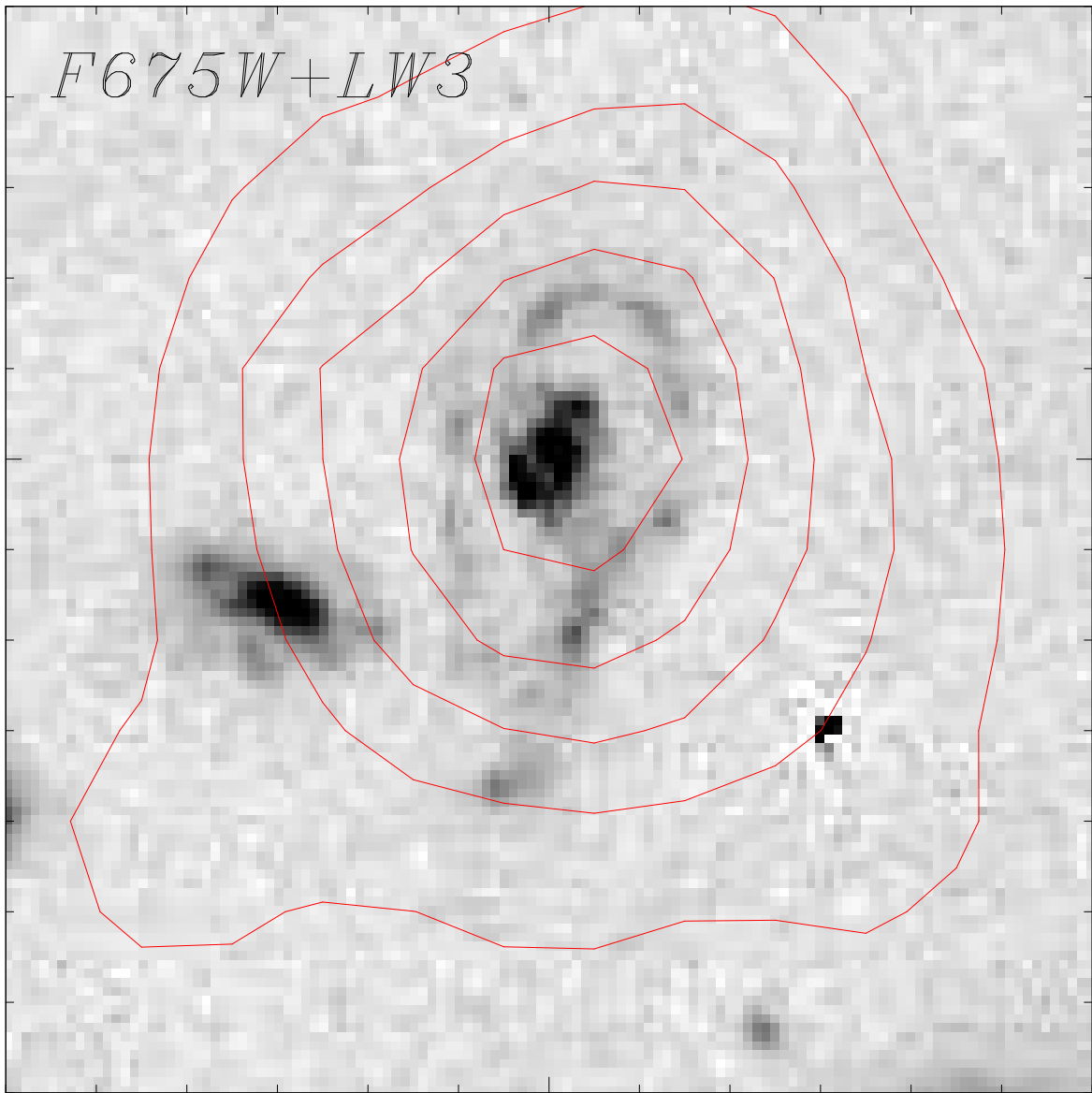
This figure "fig8a.gif" is available in "gif" format from:

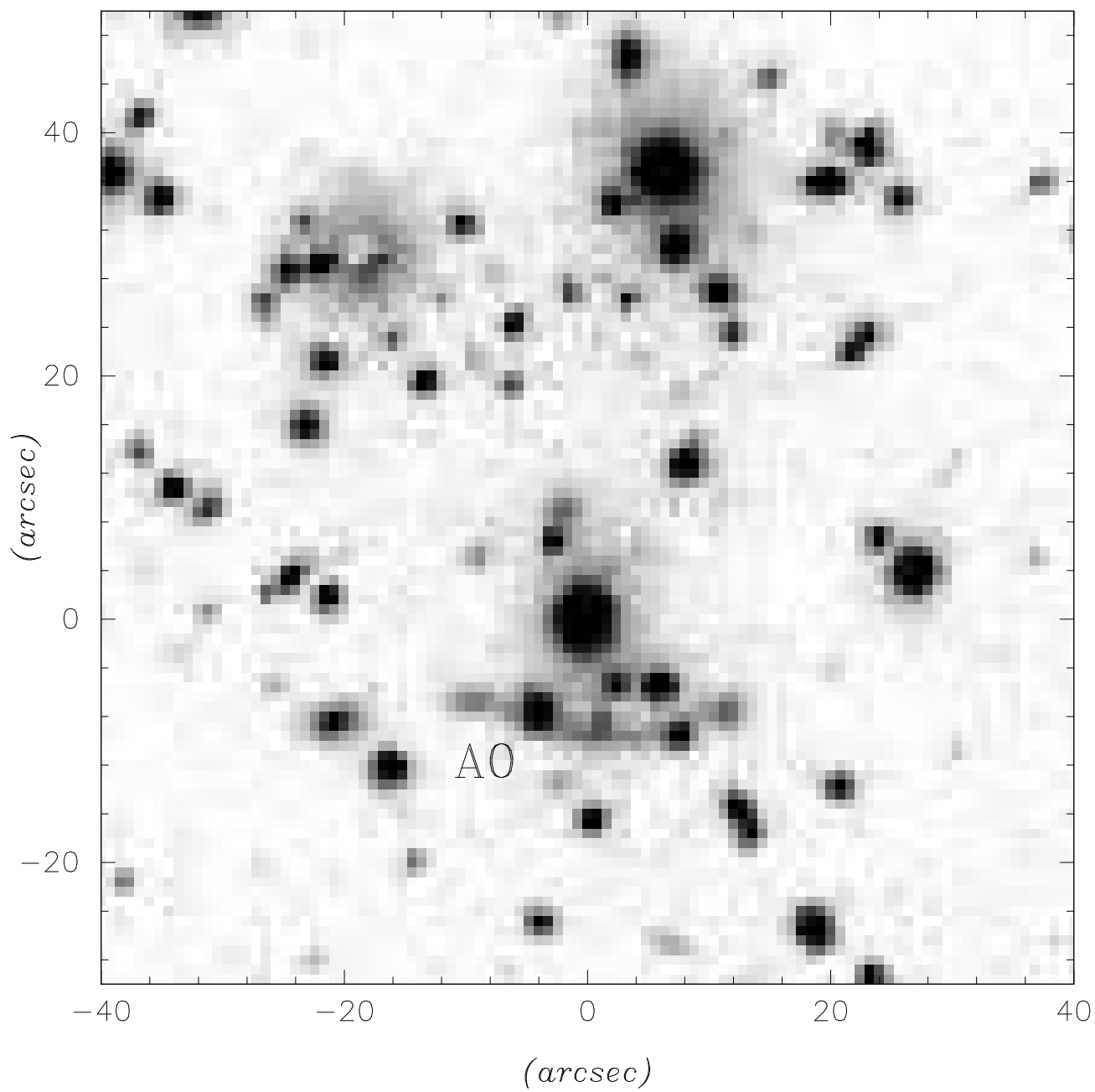
<http://arxiv.org/ps/astro-ph/9905009v1>





F675W+LW3





This figure "axj2019.gif" is available in "gif" format from:

<http://arxiv.org/ps/astro-ph/9905009v1>

This figure "ms2137.gif" is available in "gif" format from:

<http://arxiv.org/ps/astro-ph/9905009v1>